Study of Non-genetic Variability and Heritability of Pheromone Signaling in *Saccharomyces Cerevisiae* on a Microfluidic Device

by

Mani Hamidi

B.S.c., The University of British Columbia, 2012

A THESIS SUBMITTED IN PARTIAL FULFILLMENT OF

THE REQUIREMENTS FOR THE DEGREE OF

MASTER OF SCIENCE

in

THE FACULTY OF GRADUATE STUDIES

(Genome Science and Technology)

THE UNIVERSITY OF BRITISH COLUMBIA

(Vancouver)

August 2012

Abstract

Clonal populations of cells exhibit variability in gene expression despite genetic identity. Single cell technologies have helped identify various sources of such variability. Intrinsic noise in biochemical reactions as well as variability introduced by cell cycle progression and division have been suggested to play a significant role. However, there is a paucity of experimental platforms that can simultaneously measure gene expression and track cell cycle and division through multiple generations in a fully automated fashion. In this thesis I describe a microfluidic-based approach for performing such studies which integrate high-resolution live cell microscopy and automated image analysis to track lineages of multiple yeast strains for up to 8 generations in temporally and chemically controlled environments. This technology is applied to the quantitative study of non-genetic inheritance of the pheromone mitogen activated protein kinase signaling response. These studies demonstrate that the capacity to respond to pheromone is non-genetically passed on to progeny and that this response correlation is maintained between cells that are multiple generations apart. Deletions in the pheromone pathway were found to affect the strength of these correlations. While *Δfus3* cells were the most correlated of all screened strains, *Δste50* elicited dramatic asymmetry in response between mothers and their daughters leading to highly heterogeneous phenotype. Comparing expression with cell cycle phase and cell age, we present a previously unrecognized role of FUS3 in cell cycle regulation and reveal the pathway's sensitivity to asymmetric division in the absence of STE50. Our results contribute to the understanding of the origins of heterogeneity in a monoclonal population and elucidate the role of division processes and the cell cycle in giving rise to this cell-to-cell variability.

Preface

The work presented in this thesis is the subject of a manuscript, co-authored by Marketa Ricicova, Mani Hamidi, Adam Quiring, Antti Niemisto, Eldon Emberly and Carl Hansen, which is currently under preparation for publication. I am second author on this manuscript. My contribution to this work was in the design of experiments and analysis and interpretation of raw data produced from the microfluidic device and the image analysis pipeline. The microfluidic device was designed by Didier Falconnet and published previously[1]. Marketa Ricicova carried out the strain construction, chip fabrication and experimental procedures. She also helped me in experimental design and interpretation of data. Antti Niemisto developed the image analysis and lineage-tracking pipeline. Adam Quiring integrated the microscopy platform with a LabView interface and optimized the image analysis pipeline. Dr. Carl Hansen and Dr. Eldon Emberly supervised this work.

I wrote all of the sections in this document, except sections 2.2-2.4: Marketa Ricicova wrote sections 2.2 and 2.3 and Adam Quiring wrote section 2.4.

Table of Contents

List of Tables

List of Figures

List of Abbreviations

Sst – Supersensitive

Kss – Kinase suppressor of Sst2

GPA – G-protein alpha subunit

Msg – multicopy suppressor of GPA1 deletion

Fus – Fusion

Ste – Sterile

Far – Factor arrest

Ptp – Protein tyrosine phosphatase

Mpt – Multicopy suppressor of Pop Two

PRE – Pheromone responsive element

MAPK – Mitogen activated protein kinase

GTP – Guanosine triphosphate

GAP – GTPase activating protein

Acknowledgements

Thanks to Marketa Ricicova for her invaluable support on and off the project, Adam Quiring for technical help with setup and image analysis pipeline, Carl Hansen for critical feedback, funding and supervision, Eldon Emberly for guidance, feedback and supervision, CIHR Operating Grant and NSERC CREATE for funding, and Ivan Sadowski, Chris Loewen, and Anupam Singhal for useful discussions. Thanks to my family for their personal support throughout the course of this work.

Chapter 1: Introduction

Synopsis

In this work I describe the use of a microfluidic platform to study the source of heterogeneity in signaling in the pheromone pathway of Saccharomyces Cerevisieae (hereon referred to as yeast). In the first chapter I review 3 domains of research that form the foundation of the methods used and the hypothesis and questions addressed in the remaining chapters. These 3 areas are a review of (a) pheromone signaling in yeast, (b) microfluidic and fluorescent microscopy technologies used for single cell analysis, and (c) experimental and theoretical results in understanding the sources of non-genetic heterogeneity.

In 1.1 I review important molecular interactions in the pheromone pathway, from initiating events at the membrane to downstream activity in the nucleus. While such detailed mechanistic understanding highlights the success of classical genetic approaches that use bulk measurements, more recent single cell methodologies demonstrate novel insights into unattainable with traditional approaches. Fluorescent microscopy and microfluidics technologies, such as the platform discussed here, are an integral part of these single cell techniques and are reviewed in 1.2. One of the important applications of single cell methodologies has been in understanding the sources of non-genetic heterogeneity. Fluorescent proteins and microscopy in particular facilitated experimental tractability of this topic leading to a large array of studies reviewed in the 1.3.

Finally the motivation, and hypothesis, for our research and an outline of our results will be presented in 1.4.

1.1 The yeast mating pathway as a model signaling system

Mitogen activated protein kinase (MAPK) pathways are three-tiered kinase cascades, which carry out information from cell surface to nucleus and orchestrate diverse cellular decision making processes. These decisions include differentiation, and survival, with downstream effects on central cellular physiology including cell cycle progression, cell morphology, gene expression and metabolism. In yeast, the MAPK cascade is implicated in 5 distinct sensory pathways: mating, nutrient deprivation, osmo-shock, sporulation and cell-wall integrity [2]. The first three pathways share many of their MAPK components in common, yet can respond with high fidelity to each pathways' triggers without spillover in response into other sister pathways. The nutrient deprivation induces cells to differentiate into elongated cells, which grow rapidly in a connected chain through the medium to forage new environments. The osmo-shock pathway responds to high osmolarity in the environment by production of glycerol amongst other stress related responses in order to counteract this stress. The focus of this study is the mating pathway, which allows haploid cells to mate with the opposite mating type to form a diploid cell.

Yeast exists as both a diploid and a haploid form. Haploid yeast use the mating pathway to detect and locate both direction and distance of the opposite mating type. To facilitate this, each mating type produces and excretes a short pheromone peptide (termed the alpha-factor or the a-factor depending on the mating type of the cell) which act as a ligand for receptors on the opposite cell type. The mating pathway network therefore acts as a decision-making module, which has to decide on whether or not to produce "shmoo" projections and in what

direction to produce these features in order to enhance the likelihood of meeting shmoo projections of the opposite cell type. Contact between shmoo projections of opposite haploid cell types (termed MAT-a and MAT-alpha) results in the fusion of the two haploid cells into one diploid cell [3]. Given the high metabolic cost of such a decision, involving transcription of hundreds of genes and halting the progression of the cell cycle, intricate genetic regulatory motifs have evolved to tune the decision-making process and achieve optimal mating and minimal response to spurious signals. These regulatory motifs equip the pathway with a number of network properties such as ultrasensitivity* [4], bistability† [5], optimal information transfer capacity [6], recovery [7], signal fidelity [8], and regulated variability [9]. The relative ease with which yeast can be manipulated and studied has facilitated the quantitative study and characterization of such features. In addition to providing a readily manipulated and measured model of basic network properties, there is high conservation of MAPK components and motifs in higher organisms, including mammals, making the yeast pheromone pathway an archetype for signaling pathways in higher organisms with relevance in normal development and disease. Thus, the yeast pheromone response pathway has been the focus of intense study and is likely the best characterized MAPK signaling pathway. Despite these efforts a quantitative and predictive model of the mating pathway remains elusive and there are many features of pheromone response, such as cell-to-cell heterogeneity, that are unexplained.

---

* Property of dose-response curves with a steep transition from an "off" state an "on" state, not exhibited in simpler Michelis-Menten type reactions.

† Property of dynamical systems, where two different steady states can be occupied at a given input parameter depending on the system's history.

1.1.1 A run-through of the pheromone pathway in yeast

At the top of the pathway is a receptor that binds the alpha-factor as a ligand, activating the receptor. Then a set of membrane proteins transduce the activated receptor signal to the MAPK module that consists of three protein kinases (the MAPKKK, MAPKK and MAPK respectively). Through a series of phosphorylation events these kinases relay the signal down to the nucleus where the MAPKs relieve inhibition of the transcription factor responsible for activating pheromone responsive elements (PRE). The proteins involved at each of these steps are described in detail in this section.

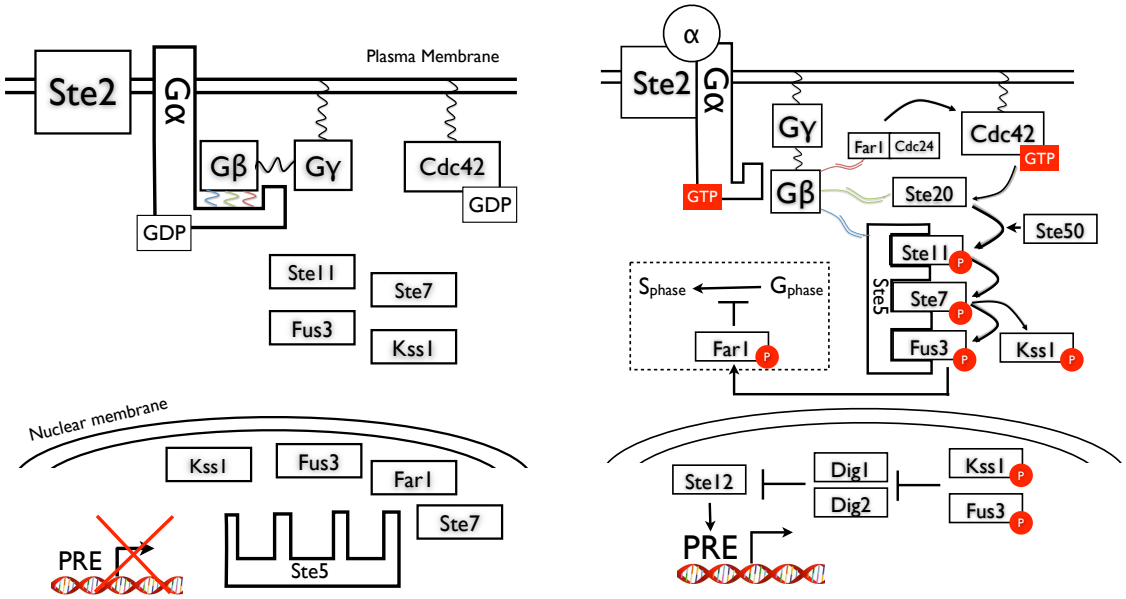

Figure 1-1 Schematic of pheromone pathway in yeast: Left – the pathway in basal state where no pheromone is bound to the receptor Ste2. The G proteins and the kinases are in an unphosphorylated state and no transcription takes place. Right – activated pathway upon alpha factor binding to Ste2. Phosphorylation of G-proteins and kinases relays activity at the membrane to the nucleus resulting in the transcriptional response. Hundreds of genes with the pheromone responsive element (PRE) sequence in their promoter region are activated, as inhibition on their transcription factor Ste12 is alleviated. The cell cycle is also halted at G1 mainly via Far1 inhibition of CDK activity.

Membrane events

The receptor responding to alpha-factor is Ste2, a G-coupled protein with a 7-trasnmembrane domain. Ste2 undergoes conformational change upon binding with alpha-factor, resulting in the release of its inhibition of the adjacent G-protein. The G-protein involved in mating pathway is a 'large' heterotrimeric G-protein consisting of 3 subunits: α, β, and γ. Activated receptor induces the Gα (Gpa1) subunit of the G-protein to exchange GDP for GTP and in doing so dissociate from the Gγβ subunits of the G-protein. The Gγ subunit keeps the Gβγ subunit bound to the membrane by covalent interactions with lipid membranes, while regions on the Gβ subdomain that were covered when bound to Gα now freely interact with a number of different effectors which help to carry on the response [10,11]. These effectors are the Ste5-Ste11 complex, the Ste20 protein kinase, and the Far1/Cdc24 complex. These interactions facilitate the spatial co-localization of Ste11 (MAPKKK) and its activator Ste20 near the active receptors, thereby connecting cytosolic signaling with the ligand-receptor activity at the membrane [3].

The scaffold protein, Ste5, acts as a vessel for Ste11 to bring it near the membrane through its affinity for Gβ. Similarly, Far1 acts as a carrier protein, which strongly binds to Cdc24, and through interaction with Gβ, brings Cdc24 to the site of membrane activity [12]. The importance of the presence of Cdc24 here is that it acts as a guanine nucleotide exchange factor (GEF), which activates yet another G-protein - Cdc42. This membrane bound protein is responsible for activating Ste20, which is central to pathway activity as it activates the first MAPK in the cascade. While the Far1/Cdc24

activity is dispensable for initiating signaling (due to the presence of sufficient levels of basally active Cdc42), it is essential for a proper chemotropic response [13].

Cytosolic events and the MAPK module

The three-tiered MAPK module of the pathway consists of Ste11, Ste7 and Fus3 which acts in a parallel role to Kss1. Auto-inhibitory function is a recurring theme in all the kinase proteins in the pathway (Ste20, Ste11, Ste7, Fus3 and Kss1): a kinase is activated when the auto-inhibitory domain is phosphorylated, alleviating its repression of the kinase domain of the protein [14-17]. Ste11 activates Ste7, which in turn activate Fus3, and Kss1, which upon (either single or dual) phosphorylation are transported into the nucleus where they yield a transcriptional response.

The initial phosphorylation of Ste11 by Ste20 takes place with the aid of the protein Ste50, which through interaction with Ste11's SAM domain makes the activation loop of Ste11 more accessible to Ste20, thereby facilitating its phosphorylation [18]. While the mutant *Δste50* isn't completely sterile, depending on the strain background the response can be up to 100 fold reduced [3]. As mentioned above, the scaffold protein Ste5 facilitates activation of Ste11 by bringing it closer to Ste20;. It also facilitates the activation of Ste11's target, Ste7, by co-localizing the two proteins close to each other on itself. The role of Ste5 in facilitating Ste7 activation by Ste11 is essential, as Ste7 is unable to bind to Ste11 without aid. While Ste5 also binds Fus3 and Kss1, contrary to Ste11-Ste7 interaction, Ste7 can bind and activate these proteins without the help of Ste5 with high affinity [19]. The role of Ste5 interaction with Fus3 is therefore not in the activation of Fus3 or even the sequestration of the signaling from cross-talk with other pathways (which share the Ste11 component) [20]. Instead, the interaction seems to be

critical in facilitating ultrasensitive and chemotropic response of the pathway by modulating the dynamics of Fus3 activity [4].

Nuclear events and transcriptional response

Phosphorylated and active Fus3 and Kss1 instigate the transcriptional up-regulation of more than 100 genes involved in mating [21]. A large portion of this activity is mediated by the transcription factor Ste12 which is known to be required for activating transcription of many of these genes. Ste12 binds to a DNA motif called the Pheromone Response Element (PRE) [22]. The mechanism by which Fus3 and Kss1 activate Ste12 is currently understood to be through direct phosphorylation of Ste12 itself and/or its inhibitors Dig1 and Dig2 [23]. Both Kss1 and Fus3 are able to activate Ste12, as evidenced by the observation that single deletions of either gene are tolerated by the pheromone pathway. However, only Fus3 is capable of phosphorylation of Far1 which leads to arrest in cell cycle and is necessary for successful mating[24]. While Far1 is central to cell cycle arrest via pheromone, Far1-independent mechanisms of arrest have also been proposed (See section 1.1.2.1) The kinase Kss1 is also the main kinase involved in the nutrient deprivation, or "filamentous" response, where under nitrogen limitation the cells exhibit an elongated invasive growth phenotype, and grow in a chain-like manner; this behavior has been interpreted as a foraging mechanism that allows cells to search for richer micro-environments [23]. While Kss1 was initially thought to serve a redundant role to Fus3 in the pheromone pathway, it has been shown that it is actually important in chemotropic response of the mating pathway and bi-stability in PRE expression at lower input concentrations of pheromone [5].

Pathway regulation

Upon pheromone pathway activation both positive as well as negative feedback and feed-forward loops modulate signaling at various positions along the pathway. This takes place both transcriptionally as well as through phosphorylation of regulatory substrates. The protease Bar1, which degrades the alpha-factor peptide is transcriptionally up-regulated upon pheromone induction, and is secreted to the extracellular space resulting in reduced sensitivity of the cell to pheromone. This makes the cells more immune from response to a transient or spurious presence of pheromone in the environment [3,25]. At the receptor level, signal attenuation occurs by phosphorylation, ubiquitination and endocytosis of alpha-factor bound receptor Ste2 [3,26]. Up-regulation of Gα acts as another negative control on the pathway [27,28]. Perhaps the most important regulator of pheromone signaling is Sst2, which acts as a GTPase, helping to hydrolyze the GTP to GDP on the alpha subunit of the G-protein, thereby inactivating it. Cells lacking Sst2 exhibit hypersensitivity to pheromone [29,30]. The up-regulation of Sst2 makes it the most prominent negative regulator of the pathway, yet it has also been shown to play a secondary signal-promoting role that helps align receptor occupancy to downstream response [6]. Another significant negative regulator of the pathway, which plays an essential role in recovery from pheromone response in the absence of mating, is the phosphatase Msg5. Unlike the regulatory mechanisms mentioned so far, this action occurs lower down in the pathway at the Kss1/Fus3 level. Msg5 (along with the less prominent Ptp2/Ptp3) is positively regulated (transcriptionally) upon signaling and is responsible for resetting the kinases of the pathway to their ground states [7,31]. While most of these regulatory mechanisms were negative in nature, there are positive motifs in the pathway as well. For example, the transcription factor Ste12 is known to bind to its own

promoter, thereby acting as a positive feedback loop, while Fus3 expression itself is also upregulated under pheromone signaling [32].

Regulation of component localization is also an important regulator of the pathway [33]. For example, Ste5 is mainly contained to the nucleus in the absence of pheromone and exported to the cytosol once the pathway has been activated [34]. Far1 localization is similar to Ste5 in that it is exported to the cytosol upon pheromone activation [12]. Other proteins however such as Fus3 and Ste7 exist in both nucleus and cytoplasm at all times [34]. On the other hand Ste11 is mostly kept outside the nucleus while Kss1 is mostly nuclear [34,35].

Here I reviewed some of the major regulatory motifs in the pheromone response pathway mainly to serve as background for the data I will present in the results and discussion chapters. Due to space constraints a discussion of many regulatory motifs is not possible here. These include, mechanisms of control over nuclear shuttling and degradation of pathway components [36], and regulation of Cdc42 by GTPase-activating proteins (GAPs). A number of review articles on the pathway can be referred to for further information on these facets of the pathway [3,27,33].

1.1.2 Cell cycle coupling of the pheromone pathway

For fusion of two haploid cells into a diploid to be successful, cells must ensure synchrony and an appropriate number of chromosomes in each cell before they fuse. This requires appropriate orchestration of signaling and cell cycle progression. To ensure this, regulatory mechanisms have evolved to tightly couple the cell cycle pathway to the pheromone pathway. This coupling takes place in both directions, meaning that the cell cycle has mechanisms to control the extent of MAPK signaling, while signaling directly influences the proliferative capacity of the cell cycle.

1.1.2.1 Signaling modulates cell cycle progression

Pheromone induction results in cells arresting in their cell cycle at START (the G1 to S phase transition). The primary mechanism of this arrest is through Far1p, which is thought to inhibit the CDK/cyclin complexes' upon phosphorylation by Fus3p [37-39]. There has also been some evidence for Far1-independent mechanisms of cell cycle arrest [40-42]. Unlike Far1-dependent arrest however, the mechanisms are thought to be less direct, through repression of CLN1, CLN2 and CLB5 transcription rather than direct regulation of CDK/Cyclin complexes [40].

In the event that mating does not occur, cells need to eventually release from arrest and continue with their regular haploid growth. Negative feedback mechanisms mentioned in the previous section play a crucial role in reverting signaling to basal levels, even in the presence of pheromone. In addition to these mechanisms however, direct proliferative regulation of the cell cycle also takes place through the signaling pathway. Both Fus3p and Kss1p have been found to upregulate CLN3 and PCL2 activity which promote budding [40]. Fus3p can also up-regulate Mcm1p which is a transcription factor that activates genes required for G1 progression [40]. These interactions are particular to activated forms of Fus3 and Kss1, and therefore are functionally implicated in recovery from pheromone response. The inactive form of Fus3 has been found to affect cAMP/RAS signaling through interaction with Cdc25 which indirectly ties Fus3 to cell proliferation [43]. This function of Fus3 however is related to the stress-response and survival and is therefore not considered central to pheromone regulation of the cell cycle.

1.1.2.2 Cell cycle inhibits signaling

All the inhibitory mechanisms noted above act to halt the cell from progressing into DNA synthesis phase (S phase) upon stimulation by pheromone. This is done to ensure appropriate number of chromosomes upon fusion. For cells that have already committed to DNA synthesis at the time of stimulation alternative mechanisms are in place to quench signaling and avoid untimely fusion [44]. While CDK/Cln2 complexes are found to modify Ste20 in the pathway [45], the only mechanism by which cell cycle inhibits signaling has been found to be via CDK/CLN phosphorylation of Ste5 [46]. The localization of this molecule at the membrane is essential for its function (see above), and was found to be facilitated via affinity towards both Gβγ subunit and with the phospholipids in the plasma membrane [47]. It is the latter interaction which CDK/Cln hampers: phosphorylation of Ste5 by CDK/Cln at multiple sites on the protein, results in accumulation of negative charge inhibiting Ste5 affinity to phospholipids of the plasma membrane and therefore signaling [46].

In summary, the mating pathway in yeast has been heavily studied as a prototype for signaling pathways in all eukaryotes. A lot of insight into molecular mechanisms of the pathway has been gained using classical approaches and techniques in genetics and biochemistry (northern/western blotting, phenotype characterization of mutants, etc.). Most of these techniques however are applied at a population level, and ignore variability that might exist at a single cell. With the advent and availability of new technologies, single cell measurements have become more of a routine. In the next section, the development of several of these technologies and their impact on biology and study of signaling is reviewed.

1.2 Single cell technologies

While bulk measurements on cell populations have proved very fruitful and continue to be used, a more quantitative and systems level understanding of biology requires probing at a single cell resolution. Modern fluorescent microscopy, coupled with genetically encoded fluorescent reporters, provides a natural and high-throughput method for quantitative real-time single-cell analysis. Emergence of several technologies has lead to an increase in the throughput and flexibility of such studies. An expanding range of fluorescent proteins and probes has provided a means to study molecular events with single cell resolution. Advance and availability of image processing and computational resources have made the analysis of the data produced from these methods more automated, quantitative and higher in throughput. Finally, micro-fabricated devices have allowed for the precise handling and immobilization of single cells, as well as dynamic control over their environments. Developments in fluorescent microscopy and microfluidics, and their application to single cell analysis, will be reviewed here as they form the technological basis of the measurements made in this study.

1.2.1 Fluorescent microscopy

Fluorescence and fluorescent microscopy were not established until early 20th century. While much was learned by looking at single cells through microscopes with the aid of various dyes and stains, application to understanding of molecular mechanisms and processes within cells did not flourish until the discovery, cloning and integration of the green fluorescence proteins (GFP) by 1992 [48-51]. The diversification of the color, stability and brightness of these proteins, through directed evolution [52-56] and the identification of alternative proteins in

nature, led to their use in virtually all aspects of cells' biology. Fluorescent proteins (FP) have since been used as quantitative reporters on promoter activity [57], protein localization [58], mRNA quantification [59], transient protein-protein interactions [6] and stochastic variations in expression [60]. FPs have proven indispensible for single cell measurements in platforms ranging from basic fluorescent microscopy of cells on glass slides [61] or flat-bottom tubes [62], to measurements on microfluidic and cytometry platforms. For example, seminal work by Elowitz and colleagues [60] using bacteria growing on glass slides sandwiched by an agar pad led to a number of studies (reviewed in the next section) giving way to an experimental measurement of noise in gene expression amenable to mathematical analysis. Similar setups have been used with yeast to measure non-genetic heritability and its effect on signaling and gene expression [63].

Roger Brent's group improved on the limited throughput of these simple setups by establishing a platform where yeast cells are grown in flat-bottom tubes and subject to imaging at high throughput [62]. Using this setup they measured time-scales of molecular interactions in the pathway [6], counting of molecular numbers with high accuracy [64], and quantification and classification of noise in the signaling process [9]. These studies have led to important insights into biology of pheromone signaling, highlighting the importance of high throughput single cell resolution analysis.

However, difficulty with maintaining cells in a single focal plain as they grow, and the impracticality of changing the environmental conditions as the cells are imaged pose serious limitations on these methodologies, particularly in the study of signaling dynamics. Microfluidic devices can address these problems and are emerging as an important tool in probing molecular mechanisms in cell biology. The development of the field of microfluidics

as well as some important microfluidic devices used to study signaling in yeast are reviewed in the next section.

1.2.2 Microfluidic technologies

Microfluidic devices are miniaturized fluid handling platforms featuring channels and other features with length scales typically ranging from ~1-1000 microns. Building on lithographic processing methods developed for the integrated chip industry, the first of these devices were made from etching and/or using photolithography techniques on hard glass or silicon substrates [65]. These devices, while suitable for application such as electrophoresis, provide only limited and complexity due to difficulties in the fabrication of sealing valves within hard materials. By comparison, the microfluidics technologies used here are made using an alternative moulding technique to create "soft" elastomeric chips. This method, originally pioneered by George Whitesides at Harvard using polydimethylsiloxane (PDMS) has now become the most pervasive method of microfluidic fabrication and is referred to as the "soft lithography" technique [66-68]. Briefly, photolithography is used to make a mold on silicon wafers using photosensitive "resists". The mold is then used for fast and cheap creation of devices by replica moulding in PDMS.[68] PDMS, unlike glass or silicon, is soft, gas permeable, and has desirable optical properties for microscopy. In 2000 Unger et al. extended this approach by developing multi-layer soft lithography [70,71], allowing for the rapid prototyping of devices with integrated membrane valves at densities approaching 10,000 per square centimeter. Micro-valves allow for much greater control over fluid flow on the device and hence higher versatility in design potential and functionality [71-73]. Several

groups have applied the Soft Lithography and MSL technique to making live-cell imaging devices suited to quantitative analysis of various cell types ranging from bacterial to mammalian. A subset of these devices and the main biological findings from them are discussed below, with emphasis on yeast signaling or studies of non-genetic variability.

Microfluidic devices for on-chip cell culture

Balaban et al [74] used a microfluidic device, to monitor bacterial growth and infer the stochastic switching of bacteria between a persistent and an anti-biotic sensitive state. Their device allowed for restricted growth of bacteria in narrow lanes of PDMS in one layer, and dynamic control over their environment through a second layer. They demonstrated applicability of microfluidics to the important problem of non-genetic variability in mono-clonal populations. The Quake lab and Levchenko's lab also used microfluidics to study bacterial growth, but in the context of biofilm formation [75] and quorum sensing [76]. Altogether, these groups established important facets of single cell microfluidic culturing such as the use of PDMS to restrict growth of cells [74], dynamically control the growth media [74,76], or use of valves and MSL architecture to run multiple experiments on the same device [75]. However, difficulties in the imaging and tracking of cells through time implied that the resulting data sets provided information about the whole population rather than individual cells.

Addressing this limitation, the Hasty lab developed a simple one-layer device inspired by Tesla's valvular conduit [77], and exploiting high elasticity of PDMS as in Levchenko's device. They trapped cells in a 4-micron high channel that forces the cells (diameter > 5 microns) to stay in a monolayer while they are imaged [76], facilitating automated segmentation and tracking of single cells. Similar to Levchenko's design, an adjacent flow channel (8-microns

high) perfused the cell environment with fresh media enabling log phase growth for more than 24 hours. They used this device on monitoring expression of fluorescent proteins regulated by synthetic genetic networks such as a tunable oscillator [78] and also to measure degradation rates of fluorescent proteins with E-coli degradation machinery integrated into yeast [79]. They also were able to monitor growth and cell cycle progression in single cells and determine their influence on the dynamics of protein concentration in a cell [80]. Another important contribution was to probe a metabolic pathway in yeast by subjecting it to periodic stimulation [81], introducing a new way of studying a system not feasible with traditional methods. This ability to attain single cell data under dynamically changing environments with microfluidics was soon exploited by other groups.

Charvin and colleagues made a multi-layer device for yeast similar to what Balaban made for bacteria where one layer was used for growth of yeast in a monolayer, while the other used to change the media surrounding the cells [82]. Furthermore, the authors fused a fluorescent molecule to a budneck (septin) protein to help track lineages of cells with the help of automated computer segmentation of the images. The authors first used this device to characterize production, maturation and degradation rates of a fluorescent protein (Venus) [82]. They then periodically induced the production of Cln2 (in *cln2* mutant cells) and orchestrated a synchronized division of the population. Cross, Siggia and colleagues went on to use this setup to gain important insights into cell cycle progression in yeast. These included demonstration of phase locking of the cell cycle and insights into size control [83-85]. Furthermore, this technique marked an important advance in the capability of microfluidic live cell imaging, as lineages in addition to single cells could be tracked. Weitz's group, also inspired by Balaban's design, made a one-layer device with lanes that would restrict yeast

growth to lanes to help with lineage tracking without the aid of fluorescent marker at the bud-neck [86]. They used the device to make a crude measurement of the time-scales of variation in a number of different proteins and found them to vary significantly.

The success of periodic stimulation in understanding regulatory networks was demonstrated in the cell cycle by Cross and colleagues, while van Oudenaarden's lab applied similar methodology to the HOG (high osmolarity growth) [87] to elucidate feedback dynamics in that pathway. All of these three setups shared the limitation of low throughput.

The work here is based on devices produced in the Hansen lab that removed this limitation in two fundamental ways [1,57]. Using a 2-layer architecture with valves, the devices could facilitate on-chip culture amenable to imaging in hundreds of chambers at once instead of a single chamber. Moreover, this matrix of >100 chambers could be used to culture multiple different strains under multiple environmental conditions in the same experimental run. This advance allowed for combining benefits highlighted by the microfluidic/single cell platforms with methodologies in classical genetic analysis, which typically involve phenotypic comparison of large numbers of mutant strains.

The first version of this device published in Taylor et al[57] consisted of 256 cell-trapping regions where cells are trapped under an actuated "sieve" valve. A sieve valve refers to a valve in MSL that when closed, still allows fluid flow in the channel it's placed over, yet traps (sieves) large particles under it [88,89]. An additional improvement in this design compared to older devices was its capacity to mix up to 8 different chemicals at the inlet with high accuracy and pump it to 32 different rows of cell traps, without cross-contamination. These features were used to probe signaling in the pheromone pathway under a number of different profiles of pheromone stimulation. Eight different mutant strains were stimulated

with pheromone pulses of various length, concentration and frequency while a GFP reporter under the pheromone responsive element (PRE) was used as the output of the cell. The comparison of different strains' response profile under different frequencies of stimulation reveals frequency-sensitivity of the cascade to the input signal. Taylor et al contend that pathway components play a functional role in modulating this frequency-sensitivity and that mutant phenotypes of deletion strains are masked in a traditional static stimulation experiment. The major drawback of this device was that the sieve valves could not perfectly hold cells motionless and therefore long-term tracking was not feasible.

Falconnet et al [1] revised the architecture to implement a matrix of low-ceiling chambers in place of the sieve valves. Moreover, cells were loaded in molten agarose, which was later cooled to polymerize on-chip in order to further minimize cell movement during imaging. Adjacent channels allowed for diffusion of media into the chamber as in Hasty and Levchenko's devices. This device could assay 8 different strains under 16 different conditions simultaneously while tracking cells over long periods of time (>12 hours). Through semi-manual lineage tracking of the cells made possible by the automated cell-tracking, the authors observed evidence for non-genetic inheritance of signaling capacity.

A slightly modified version of the device published by Falconnet et al [1] is what is used in this study for automated lineage tracking of cells (See Methods chapter).

With these modifications, the device and methodologies used in this study offer all the advantages of the devices that have been reported to-date: single cell resolution fluorescent measurements, cell tracking, lineage tracking, and dynamic control of cells' environment at high throughput and in multiple strains and conditions.

As already mentioned, dynamic control of the environment is an important feature of microfluidics platforms. While devices reviewed above demonstrate the importance of *temporal* control over the environment, several other devices have demonstrated the use of spatial control over chemical concentration in a microenvironment [4,5,90-92]. All such devices exploit a principle of diffusion, where a linear concentration gradient of solute always forms in the space between two areas maintained at different concentrations of a solute. Hasty, Levchenko and others have used such a scheme to study the chemotropic growth and response of yeast in a gradient of pheromone, unveiling functional roles of Ste5 [4], Fus3 [4] and Kss1 [5] in this feature of the pathway.

In summary, I have reviewed progress in the integration of fluorescent microscopy and advances in microfluidic platforms used for time-lapse imaging of cell cultures. With the capacity to probe cells at a single cell resolution, the study of the sources of non-genetic heterogeneity in biological systems was made possible. A historical overview of important developments in this growing area is provided in the next section.

1.3 Non-genetic heterogeneity in biology

Even before the structure of DNA was known, Delbruck formulated limitations imposed by thermal noise on enzymatic activity [93] and Erwin Schrodinger anticipated how this could interfere with the function of biological systems that macroscopically appear to operate and rely on deterministic processes [94]. Jacob and Monod's work on the *lac* operon in the 1950's identified the link between stimulus (sugar molecules), genes (the lac operon) and response (beta-galactosidase synthesis and activity), giving way to the modern conception of gene expression and regulation [95]. In parallel with these developments came measurements of

beta-galactosidase activity in clonal populations and the observation that despite genetic identity there is variability from cell to cell [96,97]. By 1976 it was clear that this phenomena was not limited to the *lac* operon and was common to a range of biological phenomena such as bacteriophage genes' expression, cell cycle periods, differentiation, flagellar motion and chemotaxis [98]. Furthermore, it was acknowledged that neither genetic nor environmental variability could be blamed for this phenotypic variability. In response to this a large body of literature probing the sources of this variability ensued, consisting of both experimental and computational efforts.

1.3.1 Experimental and theoretical studies of variability in expression

Theoretical work did not initiate until the late 1990's when gene expression via transcription and translation was modeled computationally using the Gillespie algorithm (developed in 1977 [99], and still widely used today) [100,101]. The authors found that protein production occurred in stochastic bursts and that this random variability could affect downstream processes and therefore cellular phenotypes.

van Oudenaarden's group obtained the first direct experimental evidence in 2002, relating transcription and translation rates to noise in protein levels[103]. These results supported their own theoretical analysis of gene expression in 2001[104] as well as those of Arkin et al in the 90's[100,101]. The authors used modifications of the promoter region, and the ribosome-binding site (RBS) of the reporter protein as a way to control transcription and translation rates and found that increased translational efficiency increases the noise in protein number.

Work by Serrano et al [102] further characterized variability in expression by demonstrating the reduction in variability using negative feedback control and its amplifications by positive feedback.

1.3.2 Dual-reporter experiments and classification of noise

Elowitz et al provided a general theoretical framework for experimental quantification and characterization of noise in an elegant and seminal study in 2002 that kindled wide interest in this area [60]. The authors put two fluorescent reporters of different colors under the same promoter in e-coli cells and measured the co-variation of signal between them. They recognized that noise that arises from stochasticity in the transcriptional and translational process (therefore 'intrinsic' to every cell) could be quantified by the difference between the amounts of each reporter *within cells*. On the other hand, 'extrinsic' variability introduced by factors that affect the production of both reporters (e.g. amount of ribosome in a cell), could be quantified by measurement of differences in the fluorescence of each reporter *between different cells*. The authors measured intrinsic and extrinsic noise in various different e-coli backgrounds to show that genotype can affect these properties.

These two publications from van Oudenaarden[103] and Elowitz's[60] groups set the foundation for a large number of similar studies that ensued, linking mechanistic details of expression to dynamics and quantity of noise. Blake et al observed that in contrast to bacteria, noise appeared to be sensitive to transcriptional rates as well as translation in yeast [105]. Later O'Shea's group used the dual-reporter method to complement these results in yeast and introduced a model where in addition to rate of transcription and translation, the rate of transitioning of the DNA from active to in-active state was taken into consideration [106].

Further studies[107,108] [107,108] confirmed this picture where in eukaryotes variability mainly stems from transcriptional bursts as a side product of DNA packing mechanisms and spatial organization of the chromosomes in the nucleus. On the other hand, low molecular numbers of mRNA and translational bursting sufficiently explained the variation at the protein level in prokaryotic systems [109,110]. In a study focusing on mRNA levels instead of protein numbers however, bacterial transcription was also found to be burst-like suggesting a similarity with eukoryotes[111].

The value of these experiments and their comparison with computational models has been in their ability to elucidate mechanisms of gene expression. Yet recent theoretical work by Paulsson and colleagues has shown that multiple models of expression could produce fits to the same experimental results [112]. This limitation is particularly characteristic of several features of early experimental data that suffered from at least one of the following: 1- Protein numbers were measured and not mRNA levels; 2- Protein levels were not measured in terms of molecular number but through relative fluorescence; 3- only the standard deviation of the distribution and not the distribution of protein abundances itself was used for theoretical fits. These limitations are gradually being met by new technologies and methodologies. Absolute numbers of proteins have been measured either directly [109,110]or indirectly [113]. Microfluidics has allowed for high throughput and single molecule resolution detection of protein expression [109,110] facilitating measurements of protein distributions with high statistical accuracy. Finally, fluorescent in-situ hybridization (FISH) [107]and MS2 tagging [111] methods have been used to measure mRNA levels in addition to proteins.

Ultimately these improvements should allow for an unambiguous understanding of the source of intrinsic noise and overcome limitations of dual-reporter assays and other existing methods [112,114,115].

1.3.3 Non-genetic heritability and extrinsic variability

While the large body of literature reviewed above has produced much insight into the nature and origin of intrinsic noise, extrinsic noise has been much less characterized and understood [116]. Dual-reporter methods have provided quantification of extrinsic noise and a characterization of the time scales over which it operates [113]. Other studies have demonstrated how variability in upstream elements could propagate through a genetic network and manifest as extrinsic noise for downstream promoters [117]. The lack of insight into the sources of extrinsic noise is perhaps due to its dependency on the idiosyncrasies of a particular biochemical network, making it intractable to general models. Nevertheless, extrinsic noise has been shown to dominate intrinsic variation in the pheromone pathway in yeast [9], where cell cycle position and other extrinsic factors account for most of the variability in the transcriptional response of the cells to pheromone. A destabilized GAL-network in yeast was shown to exhibit stochastic transcriptional dynamics that was determined by the abundance of a single extrinsic factor: a negative regulator of the pathway [63]. Sorger and colleagues got a similar result where they found the decision for apoptosis was dependent on variability in several proteins in the pathway[118]. Both of these works[63],[118] also showed that the cells' phenotypes were non-genetically inherited. Another recent study investigated the role of mitochondrial activity and mass in determining transcriptional rates and variability in expression [119]. After ruling out variability in RNA polymerase II as a

significant contributor to transcriptional variability, they showed that stochastic division of mitochondrial mass at division is correlated to transcriptional variability in the cells. These three experiments demonstrate how evaluating the heritability of a phenotype can shed light on the sources of extrinsic variability, partly motivating our efforts to quantify heritability of the pheromone response capacity in yeast.

1.3.4 Practical implications

There are practical implications of the study of non-genetic variability, particularly in the areas of drug resistance, evolution and the emerging field of synthetic biology. As demonstrated by Balaban and colleagues, non-genetic heterogeneity in a bacterial population can be responsible for persistence against antibiotics [74,120]. Therefore the understanding and modulation of this heterogeneity by interventional methods could have obvious application in battling infectious bacteria. Sorger and colleagues showed that genetically identical cells exhibit variable response to apoptosis-inducing signals [118]. This result is directly implicated in cancer therapy, as the signaling molecule used there is under clinical trials as a cancer treatment [121].The authors suggest how co-drugging could help reduce heterogeneity in response to the apoptosis-inducing drug and therefore help remove all, instead of only a fraction, of the cancerous cells [118,122]. From these studies it is clear that that non-genetic traits, just as genetic traits, can be selected for by pressures such as antibiotics and are therefore important for in the context of evolution of organisms just as they are in evolution of disease. While experiments in synthetic biology played an important role in the development of this field, the results will in turn have important implications in development

of synthetic circuits which aim to minimize or perhaps exploit it as in some natural systems [123-125].

1.4 Summary

In this chapter I first reviewed the molecular mechanism of signaling in the pheromone pathway as revealed by classical genetic analysis. I then showed how emerging single cell technologies are addressing a more detailed understanding of molecular pathways. Finally a body of single cell studies aiming to understand the origins of non-genetic variability was reviewed.

In this study we use automated lineage tracking on a microfluidic device to explore the sources of variability in the pheromone mating response in yeast. This goal is motivated by the status of the mating pathway in yeast as a prototype for signaling pathways in all eukaryotic organisms, and the noted practical implications of understanding non-genetic variability in biology. We hypothesize that quantification and characterization of heritability in signaling capacity will reveal the mechanisms underlying the extrinsic variability in signaling that remain poorly understood to date. Moreover, by screening 8 different deletion strains we aim to probe the role of proteins in the pathway in determining the degree of this variability.

This thesis is organized as follows: Chapter 2 provides details on the microfluidic device, the lineage tracking algorithm and some analysis to quantify the throughput and quality of the data produced on our platform. Chapter 3 provides results from a screen of 8 different strains under a transient stimulation by pheromone. By combining single cell information on transcriptional response, cell cycle progression, morphology and lineage, I show that

signaling capacity is inherited in yeast. Moreover I reveal that cell cycle progression and asymmetry account for a large portion of non-genetic heterogeneity in pheromone signaling and are modulated by pathway components. I discuss the implications of these findings and conclude in Chapter 4.

Chapter 2: Technology and Methods

Synopsis

A multi-layer microfluidic device, a fluorescent microscopy platform, and a software pipeline for automated cell segmentation and lineage tracking form the experimental system used in this study and will be described in this chapter. The genetically modified strains of yeast used in these studies, as well as the experimental protocols will also be described in detail in this chapter.

2.1 Microfluidic device

The device used for all experiments in this study is the same as that reported in Falconnet et al[1]. For details on device design, fabrication and operation refer to Falconnet et al[1]. The device design and fabrication was based on techniques in multilayer soft lithography using poly-dimethylsiloxane (PDMS, RTV-615, Momentive) [71,72]. The device has a 'push-down' geometry where cell chambers and fluidic channels appear in the bottom PDMS layer and the control layer with valves in the top PDMS layer. The cell chambers are organized in an array of 16 rows and 8 columns. A multiplexer addresses fluids from a single input port into any of the 16 rows of the array at a given time. Each column of chambers can be loaded with a different strain as each column is separated from the others by a set of valves that are actuated upon loading the device with cells.

There were slight modifications made to the device to facilitate lineage tracking. Chamber size was reduced to 434x165x2 microns, in order to fit a single chamber into two fields of view of a 63x objective. Fiduciary features were fabricated next to each chamber in order to

allow for an auto-focus procedure to be performed on each chamber. Each chamber was equipped with 8 pillars to prevent the collapse of the ceiling. The 2-micron ceiling height was achieved using SU8-2 photoresist (Microchem.). The device is plasma bonded to a 0.21-mm Schott D263 borosilicate glass slide (SI Howard Glass) compatible with 63x objective.

2.2 Experimental protocol

Yeast strains were cultured overnight in rich media and then diluted in fresh SCD (synthetic complete dextrose media with 2% glucose) and grown to exponential phase. Cells were centrifuged at 1957 x g for 2 min and concentrated in SCD supplemented with 0.2% BSA (bovin serum albumin, Sigma Aldrich) to an OD_{600} = 1 to 4 depending on the desired seeding density. Cells were then mixed 1:1 with a 3% gel of low melting agarose (Sigma Aldrich) dissolved in SCD to reach final concentration of 0.1% BSA and 1.5% agarose. We have tested that 0.1% BSA still prevented α-factor from adhering to the walls of the PDMS channels/chambers and unlike higher BSA concentrations it did not affect growth rate of cells. The suspension was vortexed to homogeneity and transferred to the microfluidic device according to the protocol described previously [1]. Before we opened diffusion valves that separate experimental chambers from feeding channels, all channels were primed with SCD supplemented with 0.5% BSA to further prevent adhering of chemicals to the PDMS walls. 100nM α-factor (ZymoResearch) and 250mM hydroxyurea (Sigma Aldrich) were dissolved in SCD + 0.1% BSA. All solutions were stored in 2ml custom adapted vials[1], connected to the device by tubing and pressurized by 2 p.s.i. air. Cells in the chip were grown at room temperature and divided approximately every 100 min which is similar to batch cultures at 30°C. Starting usually from 1 to 10 cells per chamber (OD_{600} = 1 before mixing with agarose

gel) we ran experiments over 13h before cells filled the chamber and began to stack on top of each other.

2.3 Strains

The list of strains used in this study is in the Table 1. All strains are *MATa* type and they were derived from the diploid strain BY4743 (S288C background). They are deleted for *BAR1* gene encoding pheromone protease and contain three fluorescent markers: Cdc10-YFP fusion protein that localizes in the budneck, PRE-mCherry reporter of pheromone pathway activity and ACT1pr-yECFP reporter used for cell segmentation in the image analysis.

BAR1-HphNT1 cassette for *BAR1* deletion was amplified from pFA6a-hphNTI vector [126]. Plasmid pKL973 carrying CDC10-YFP-LEU2 construct was kindly provided by K. Lee (NIH). PRE-mCherry-HIS3 cassette was amplified from PRE-mCherry vector which was made by swapping GFP in PRE-GFP vector [57] by mCherry from pBS34 plasmid (YRC) using PacI and AscI restriction sites. Vector for generation of ACT1pr-yECFP-CaURA3 cassette was constructed by cloning ACT1 promoter fragment (amplified from BY4741 genomic DNA ~600bp upstream from ACT1 open reading frame) in PvuII-HindIII restriction sites of pKT174 plasmid (EUROSCARF) upstream of yECFP coding sequence [127].

Strain name	Genotype
WT(737D)	*MATa met15Δ 0 ura3Δ 0 leu2Δ 0::*CDC10-YFP-LEU2 *bar1Δ*::HphNT2 *his3*::PRE-mCherry-HIS3 *ho::*ACT1pr-yECFP-CaURA3
far1Δ	*MATa met15Δ 0 ura3Δ 0 leu2Δ 0::*CDC10-YFP-LEU2 *bar1Δ*::HphNT2 *his3*::PRE-mCherry-HIS3 *ho::*ACT1pr-yECFP-CaURA3 *far1Δ*::KanMX4
fus3Δ	*MATa met15Δ 0 ura3Δ 0 leu2Δ 0::*CDC10-YFP-LEU2 *bar1Δ*::HphNT2 *his3*::PRE-mCherry-HIS3 *ho::*ACT1pr-yECFP-CaURA3 *fus3Δ*::KanMX4
kss1Δ	*MATa met15Δ 0 ura3Δ 0 leu2Δ 0::*CDC10-YFP-LEU2 *bar1Δ*::HphNT2 *his3*::PRE-mCherry-HIS3 *ho::*ACT1pr-yECFP-CaURA3 *kss1Δ*::KanMX4
msg5Δ	*MATa met15Δ 0 ura3Δ 0 leu2Δ 0::*CDC10-YFP-LEU2 *bar1Δ*::HphNT2 *his3*::PRE-mCherry-HIS3 *ho::*ACT1pr-yECFP-CaURA3 *msg5Δ*::KanMX4
ptp2Δ	*MATa met15Δ 0 ura3Δ 0 leu2Δ 0::*CDC10-YFP-LEU2 *bar1Δ*::HphNT2 *his3*::PRE-mCherry-HIS3 *ho::*ACT1pr-yECFP-CaURA3 *ptp2Δ*::KanMX4
ste50Δ	*MATa met15Δ 0 ura3Δ 0 leu2Δ 0::*CDC10-YFP-LEU2 *bar1Δ*::HphNT2 *his3*::PRE-mCherry-HIS3 *ho::*ACT1pr-yECFP-CaURA3 *ste50Δ*::KanMX4
mpt5Δ	*MATa met15Δ 0 ura3Δ 0 leu2Δ 0::*CDC10-YFP-LEU2 *bar1Δ*::HphNT2 *his3*::PRE-mCherry-HIS3 *ho::*ACT1pr-yECFP-CaURA3 *mpt5Δ*::KanMX4

Table 2-1 Details of the strains used in this study

pKL973 plasmid, cassettes with fluorescent markers ACT1pr-yECFP-CaURA3 and PRE-mCherry-HIS3, and BAR1-HphNT1 deletion cassette were first separately transformed in BY4743 diploid strain and their proper integration in the genome was verified by PCR and/or by fluorescence microscopy. Confirmed clones were sporulated and haploid strains with individual markers were selected and consecutively crossed with each other to obtain a parental strain 737D with all three fluorescent markers and *BAR1* deletion. Additional knock-

outs of pheromone pathway genes were made by PCR gene replacement with kanMX deletion cassette amplified from pFA6a-GFP(S65T)-kanMX6 vector.

2.4 Imaging, segmentation and lineage tracking

2.4.1 Image acquisition and chip operation

The device was imaged using a Leica DMIRE2 inverted microscope and 63x oil immersion objective (HCX PL APO, NA 1.4-0.60). A Leica EL6000 light source with a high-speed shutter and mercury lamp (HXP R 120W/45C VIS, Osram) were used with three different filter cubes (Leica "YFP"; Leica "TX2"; Semrock "CFP-2432A-LSC-ZERO") for fluorescence imaging. To minimize photobleaching, the light source was operated at minimum intensity and the numerical aperture was maximized (NA 1.4) by fully opening the objective's iris. Bright field images were captured through the YFP filter using a custom-installed light-emitting diode in place of the halogen lamp to enable quick switching between bright field and fluorescence. All images were captured with a ORCA-ER digital camera (Hamamatsu) capable of 1344x1024 pixel resolution. The microscope was fitted with a Prior Proscan III XY stage (1 mm ball screw, 50 nm encoders), enabling fast and precise scanning through the array of imaging chambers on the device, and was kept inside a rigid plastic enclosure to keep it isolated from ambient light and high-frequency fluctuations in room temperature.

Time lapse imaging and perfusion of the array were controlled by a PC running LabVIEW 7.1 (National Instruments). To set up the experiment the user selected a sub-array of chambers to be imaged, captured an image of a fiducial to be used as a template for pattern-recognition, manually located and focused on the fiducials for three chambers in the sub-

array, and calculated the x/y offset between a chamber and its fiducial. The software would then scan through every fiducial in the sub-array and capture a z-stack of bright field images, using pattern recognition (IMAQ, National Instruments) to pinpoint the fiducial's exact xy location and autofocusing by selecting the image in the stack with the lowest variance. The x, y, and z coordinates of each fiducial were stored for future reference. At this point the user could select chambers to be imaged based on the quality of the autofocus and pattern-recognition results. Typically, over 98% of all chambers in the sub-array were chosen for imaging. Finally, the user defined a time-dependent chemical condition for each row and the software began simultaneously perfusing and imaging the array.

Once imaging and perfusion began, the rest of the experiment was fully automated. Before each row was imaged, the most recent chemical sent to the row was recorded. The imaging of a row began with the YFP filter, through which all bright field and EYFP images were acquired. At each fiducial in the row, autofocusing was performed to detect any change in z-coordinate using a z-stack of 7 images at 0.5 micron spacing, following which the corresponding chamber was imaged in bright field and EYFP. The z-coordinate of the chamber was inferred by interpolating or extrapolating stored z-coordinates of nearby fiducials and offsetting this by the change detected during fiducial autofocusing. Bright field images (1x binning) were taken in focus as well as 3.5 microns above and below the focused position, and EYFP images were taken in focus at (2x binning, 200 ms exposure). In focus images were then taken of the entire row through the CFP filter (2x binning, 100 ms exposure), and finally through the TX2 filter (2x binning, 40 ms exposure), before moving on to the next row. Through the use of a high-speed shutter, the cells were only exposed to excitation light during image capture so as to reduce photobleaching and exposure to

potentially damaging high-frequency light. When imaging of the chip finished, the stored fiducial z-coordinates were updated to reflect the changes detected during autofocusing and re-imaging of the array began immediately.

2.4.2 Segmentation

The two bright field images (3.5 microns above and below the focus position) were normalized independently of each other so their pixel intensities occupied the entire range [0,1], and the difference between the two images was calculated. The diffraction patterns around the unfocused cells interfered constructively during this step, highlighting the cell boundaries while obscuring the background and cell bodies. The difference image was then thresholded using Otsu's method to create a binary image, for which the number of black and white pixels were counted. If the image was more than 50% white pixels, a second thresholding step was performed. The final thresholded image was subjected to a morphological opening to remove small objects and a morphological closing to remove small holes, giving a binary image, B_{bnd}, that represented the cell boundaries.

Next, the normalized bright field image from above the focus position was used to make a mask of the cell colonies. The image was variance-filtered, re-normalized to occupy the entire range [0,1], thresholded using 0.5 times the threshold obtained from Otsu's method, and dilated. The background of the resulting image was identified as the largest connected object in the complement image, and all black pixels that were not part of the background were filled in. The image was then eroded to give B_{col}, a mask of the cell colonies.

Individual cells were identified using two methods. The first method removed the cell boundaries (B_{bnd}) from the cell colony mask (B_{col}). This method produced some false negatives where the cell colony mask had failed to include certain cells. The second method took the complement of B_{bnd} after using a flood-fill operation to fill in the background, producing false negatives in cases where the boundaries in B_{bnd} were not completely closed. By combining the results of these two methods, a segmentation of all the cells was created. A morphological opening was then used to eliminate small or thin objects, and touching cells were separated from each other using the watershed of the Euclidean distance function of the complement image. The h-maxima transformation was used to prevent over-segmentation. The background of the resulting image was identified as the largest connected object in the complement image, and all black pixels that were not part of the background were filled in. Objects smaller than 30 pixels were removed, and large objects were removed based on a pre-defined threshold and a median threshold. This image, B_{BF}, still contained a few false positives.

To eliminate false positives, information from the CFP image was used. The CFP image was corrected for uneven illumination by fitting a quadratic surface to the intensity image and then subtracting the surface from the image. The pixel intensities were then normalized to occupy the entire range [0,1] and the image was thresholded using Otsu's method. After a dilation of the resulting binary image the number of black and white pixels were counted and, if the image was more than 75% white pixels, another thresholding step was performed. A morphological opening was performed and clumped cells were separated from each other using the watershed of the Euclidean distance function of the complement image. The h-maxima transformation was used to prevent over-segmentation. The resulting binary image is

herein referred to as B_{CFP}. Finally, the complement of B_{BF} was flood-filled, using the white pixels in B_{CFP} as start locations, and the result was masked with B_{BF}. Any cell, which touched the edge of the image, was then removed, so that analysis was only performed on whole cells. Additionally, cells within 200 pixels of the left edge (for the left FOV) or 200 pixels from the right edge (for the right FOV) were assumed to be trapped under the chamber isolation valves and so were also removed from the segmented image.

2.4.3 Cell tracking

After the cell segmentation was complete for time point t, cells and lineages were tracked from time t-1 to time t. From previous iterations, each cell being tracked had already been assigned a label I. After assigning a temporary label j to each cell in time point t, the tracking problem was posed in terms of combinatorial optimization as the classic assignment problem, where the labels from t-1 acted as agents and the labels from t acted as tasks. The cost C_{ij} of assigning task j to agent i was taken to be $C_{ij} = D_{ij} + 0.25|S_j - S_i'|$ where D_{ij} was the Euclidean distance between the centroids of the two cells, S_j was this size of cell j, and S_i' was the estimated size of cell i after accounting for cell growth over the course of one time point. This size estimation was done by assuming that cells smaller than 75% of the median cell size grow by 25% per time point, while the rest of the cells remain the same size. The cost matrix C is then modified by giving infinite cost to the following elements: Elements with $D_{ij} > 25$, Elements with $S_j/S_i' > 3$, Elements with $S_j/S_i' < 0.66$, Elements for which i is "full

grown" and $S_j/S_i' > 1.25$, Elements for which i is "full grown"[‡] and $S_j/S_i' < 0.8$, Elements for which label i has been retired.

A version of the Hungarian algorithm that was modified to work with rectangular weight matrices was used to solve the assignment problem given by the resulting cost matrix. From all of the assignments made by the algorithm, the median cost c_{med} and mean absolute deviation of costs c_{mad} were calculated. Every task j that was unassigned by the algorithm was then assigned to the agent i which gave the minimum cost if and only if (a) the cost satisfied $C_{ij} < c_{med}+3c_{mad}$ and (b) the agent i was not already assigned. All cells from time t that remained unassigned were assumed to be new cells and were given new labels. At this point, labels that had been unassigned for three consecutive time points (t, t-1, and t-2) were marked as "retired" and were avoided in future time points. The size of each cell and the location of its centroid were recorded for use in the next iteration of the tracking algorithm. For unassigned labels, the size and centroid location from the previous time point (t-1) were recorded instead.

2.4.4 Lineage tracking

Once cell tracking was completed for a given time point, information from the YFP image was used to perform lineage tracking. The YFP image was corrected for uneven illumination by fitting a quadratic surface to the intensity image and then subtracting the surface from the image. The pixel intensities were then normalized to occupy the entire range [0,1]. The budnecks were segmented using a local comparison and selection segmentation algorithm and objects smaller than 5 pixels were removed.

[‡] A cell was considered to be "full-grown" if it was at least 25% larger than the median cell size.

For each segmented budneck, the two cells touching it were investigated to see if they formed a mother-daughter pair. If one cell was at least 1.5 times the size of the other, then the larger cell was proposed as the mother. Otherwise, no pairing was proposed from the given budneck. The overlap between the budneck and the proposed daughter was recorded as a measure of the confidence in the pairing. The proposed pairing was accepted and recorded only if the proposed daughter was not already identified as a mother, the proposed daughter appeared after the proposed mother, and the proposed daughter was not already assigned to a mother with higher confidence.

If a segmented budneck touched less than two cells (or more than two cells), up to two dilations (or erosions) were performed in an attempt to find exactly two cells that overlapped with the budneck. If this was successful, the pairing process was attempted for a second time. Otherwise, no pairing was proposed from the given budneck.

Two notable changes were made to the above algorithm when the first time point was being processed. First, proposed mothers were not required to be 1.5 times the size of the daughter; merely being larger than the daughter was sufficient. Second, proposed daughters were not required to have appeared *after* their proposed mother.

In some cases, the methods described above led to new cells which could not be identified as mothers or daughters. This was often caused by inadvertent over-segmentation of a hollow cell into several pieces when the watershed function was used to separate clumps of cells. It is common for a cell to appear hollow when it contains a large vacuole. To deal with this, all new non-daughter non-mother cells were slightly dilated to include the cut lines used to separate them from their neighbors in the watershed step, effectively re-assembling the over-

segmented cell. All holes in the segmentation image were then filled before re-doing the watershed step, and the cell/lineage tracking routines were repeated for a second and final time.

Post-processing

Once cells and lineages had been tracked for all time points, the tracking data was inspected for errors and the following post-processing steps were used to either correct the suspected errors or remove the affected cells from the analysis.

Removal of transient cells

Labels that were found in fewer than three frames and not in the final frame were likely a result of false positives in the segmentation or inaccurate cell tracking. These labels were removed from the data set.

Connection of cell trajectories

Errors in cell tracking sometimes caused a cell's label to change, incorrectly suggesting that one cell had disappeared and a different cell had appeared. The Hungarian algorithm was used to match disappeared labels with newly-appeared labels to correct this mistake.

For each frame t, labels which were present in the previous frame t-1 but absent in all frames from t onwards acted as agents in the assignment problem. Labels which were present in t, absent from all previous frames, and larger than half of the median cell size in t acted as tasks. This requirement on cell size ensured that the trajectories of small, newborn cells were not falsely connected to the trajectories of pre-existing cells. It was also required that all agents and tasks have their centroids at least 50 pixels away from the edges of the image so that trajectories of labels which had recently entered or exited the field-of-view were not falsely connected. The cost C_{ij} of assigning task j to agent i was taken to be $C_{ij} = D_{ij} +$

$0.25(S_j/S_i)$ where D_{ij} was the Euclidean distance between the centroids of the two cells, S_j was this size of cell j, and S_i was the size of cell i. The cost matrix C is then modified by giving infinite cost to the following elements: Elements with $D_{ij} > 50$, Elements with $S_j/S_i > 3$, Elements with $S_j/S_i < 0.66$, Elements for which i is "full grown"[§] and $S_j/S_i > 1.25$, Elements for which i is "full grown" and $S_j/S_i < 0.8$.

The assignment problem given by the resulting cost matrix was solved using the same version of the Hungarian algorithm as was used for cell tracking. For every matching pair of labels, i and j, all instances of label j in the data set were replaced by label i, thus connecting the two trajectories.

Removal of large newborn cells and their daughters

In cases where the segmentation algorithm was unable to resolve large clumps of cells, these clumps would appear as one large cell. Cells which, in their first appearance, were greater than 1.5 times the median cell size of that frame and whose centroids were not within 50 pixels of the image edges were suspected to be a result of incorrectly-segmented clumps. These cells, along with all daughters that had been assigned to them, were removed from the data set.

Fluorescence quantitation and background correction

Before quantitation of CFP and TX2 images could be done, the uneven illumination and collection efficiency of the microscope needed to be corrected for. For each experiment, the user selected a frame with few cells to serve as an illumination and collection efficiency

---

[§] A cell was considered to be "full-grown" if it was at least 25% larger than the median cell size.

template for the entire experiment. The software used linear regression to fit a 4th-degree polynomial surface to the pixel intensities in the template image, ignoring regions in the image that the user identified as containing cells or high autofluorescence. By sampling this surface at the resolution of the fluorescence images and then dividing by the global maximum, a correction image was obtained. Two correction images were created, one for EYFP and one for TX2, and were used to correct every time point in every chamber for a given experiment.

CFP and TX2 fluorescence intensities were measured for every cell in every frame as the mean of the cell's pixel intensities (after division by the correction image). The background intensity of each image was also measured as the mean/median/mode-with-binning of all "background" pixels, where the background pixels were identified by thresholding the image using Otsu's method after normalizing the pixel intensities to [0,1].

It should be noted that all images which were involved in fluorescence quantitation had 197 subtracted from them immediately after being read from disk in order to remove the effect of the camera's dark current.

2.5 Quantification and quality of data

2.5.1 Quantification of data

After segmentation and tracking was completed, the time series for total mCherry in every cell, as well as the lineage information for every cell was then parsed for higher level analysis of the data. This step was carried out using multiple custom Python scripts [128]. First, data from the whole chip was taken, chambers with shared strain and experimental protocol were bundled, background reduction performed on every cell, and finally average

fluorescence (total fluorescence divided by cell area) was calculated at every time point before data was passed for downstream analyses. These analyses included visualization of lineage trees and expression profiles, growth curves and other analyses presented in this and future chapters.

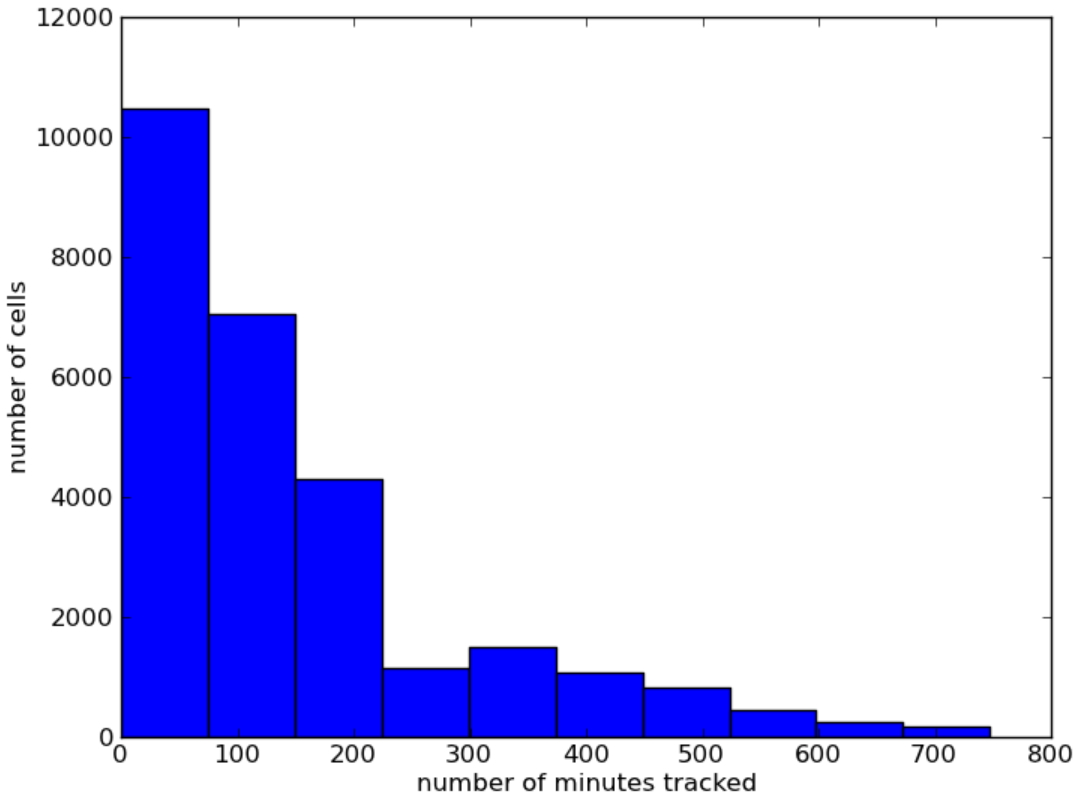

Figure 2-1 Distribution of duration of tracking single cells: 14,296 cells were tracked for more than 100 minutes which is about the length of a full cell cycle, demonstrating the throughput of the cell tracking algorithm.

Figure 2-1 and Figure 2-2 demonstrate the throughput of the cell and lineage tracking of this platform based on data from a single experiment. The distribution of lengths of times for which a cell is tracked for is shown in Figure 2-1: 14,296 cells were tracked for more than 100 minutes which is about the length of a full cell cycle. Figure 2-2 shows the distribution

of number of generations for which a genealogical tree was tracked. 13,131 cells were tracked for more than 2 generations. We have tracked up to 8 generations on our device; this is the highest throughput reported to our knowledge.

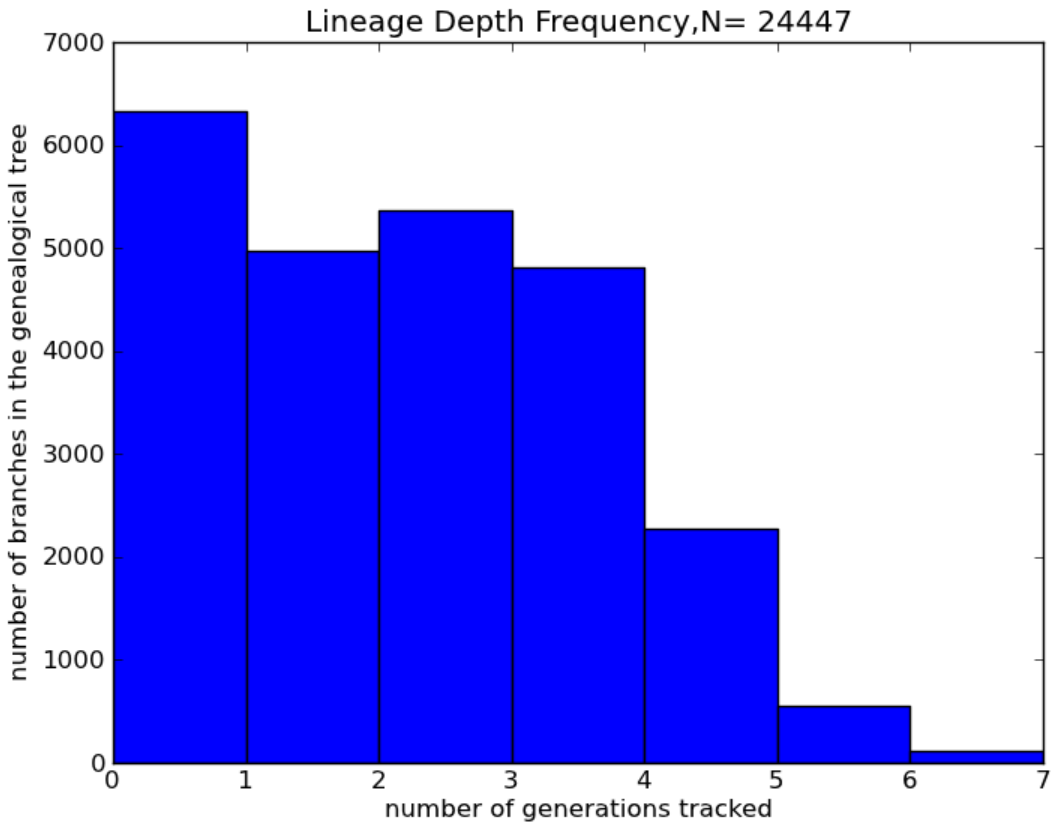

Figure 2-2 Distribution of lineage depth tracked by the algorithm: 13,131 cells' lineage was tracked for more than 2 generations, demonstrating the throughput of the lineage-tracking algorithm.

2.5.2 Quality of data

2.5.2.1 Cell-tracking and lineage-tracking errors

Due to the large throughput of the setup and the relative low occurrence of errors in cell tracking, segmentation or lineage tracking it was difficult to get direct estimates of error rates; manual tracking of cell lineages is too laborious to be a practical method of

comparison. An indirect estimate of error in lineage tracking was however provided by counting the number of cells segmented and tracked but not associated with a mother cell. Out of the total of about 27,000 cells in the same experiment as presented above, about 9,000 were mother-less; however, more than 6,000 of these were born in the very last time point in the experiment pointing to the increase in rates of error towards the end of the experiment, further complicating calculation of a simple measure of rate of error. Therefore out of about 21,000 cells tracked about 3,000 were not associated with a mother suggesting a ~14% rate of failure in detecting lineage. This type of error however is innocuous as it can be assumed that a cell appearing in the middle of the experiment without a mother associated with it, is either coming from outside of the field of view from the periphery of the chambers or that the algorithm was unable to identify a mother despite it being in the field of view. In contrast, more problematic mistakes such as mislabeling of a cell mid-tracking, or incorrect mother-daughter association of two cells, are not obvious and also difficult to quantify. While some such errors reveal themselves in downstream analyses as outliers and can be removed, others may remain hidden. The low rates of occurrence and the performance of multiple replicate experiments on the same device help to mitigate the adverse effects of such errors.

Even if a cell is correctly segmented and associated with a mother upon birth, the time of its birth is subject to technical noise. The recorded time of birth for a cell is the time point when a cell is first segmented and labeled as a cell. The fundamental limit on the accuracy of this measurement is set by the frequency of imaging which is about 11 minutes or about a tenth of a cell cycle.

2.5.2.2 Noise in fluorescent measurements

At every time point the total fluorescent intensity of a cell in both the mCherry and the CFP channels are recorded. Other than the number of fluorescent proteins within a cell other factors affect the brightness of a single cell. While deviations from the focal plane was initially suspected to be a significant source of error, comparison of images from one time point to another showed that fluctuations existed even in background fluorescent signal which should not be sensitive to z-position of the stage. From this it was suspected that fluctuations in the intensity of the excitation beam were contributing to noise in fluorescent measurements. According to this hypothesis one would expect that (a) the fluctuations in the mCherry and CFP channel within each chamber are correlated and (b) the correlation between CFP and mCherry signal of *different* chambers drop as the time between the imaging of the two chambers increases. Figure 2-3 and Figure 2-4 show that both of these observations are made experimentally, confirming that fluctuations in the intensity of the mercury bulb account for most of the noise in fluorescent measurements.

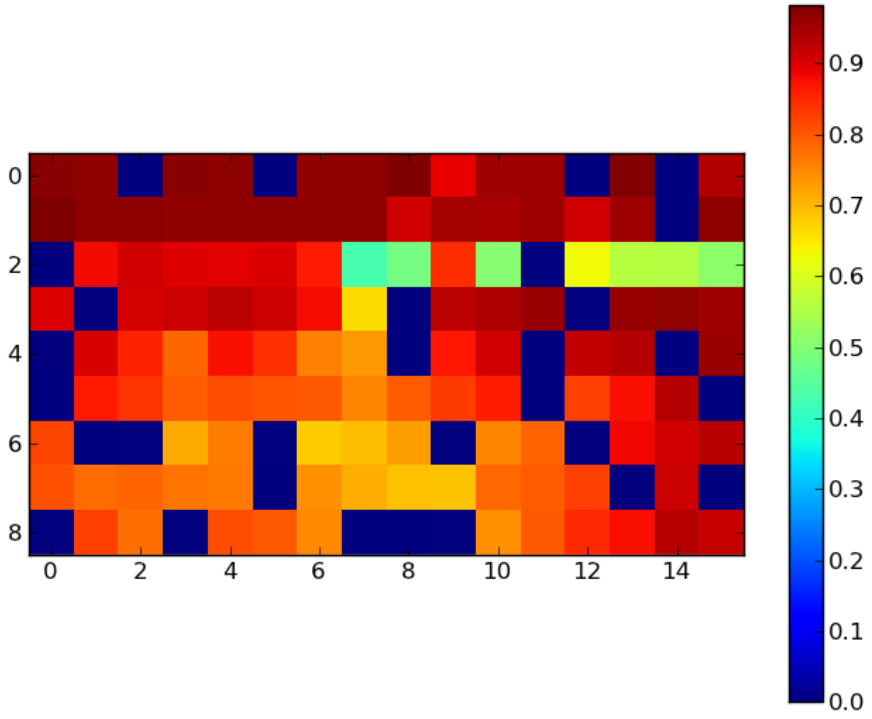

Figure 2-3 Fluctuations in mCherry and CFP background signal are correlated within every chamber: Each element in the grid corresponds to half a chamber on the device. The color indicates the correlation coefficient as indicated by the side bar. The blue elements were chambers that were not analyzed by the program. This data is consistent with the hypothesis that fluctuations in imaging from one time point to another are due to fluctuations in the excitation beam coming from the mercury lamp.

The matrices in Figure 2-3 and Figure 2-4 represent all fields of view imaged on the chip (16 columns and 8 rows), where in Figure 2-3 the correlation between the CFP and mCherry signal from the same chamber is shown and in Figure 2-4 the correlation between the mCherry signal of the top-left chamber with the CFP signal of each of the other chambers is shown. The CFP signal from the chambers at the bottom of the chip de-correlates from the mCherry signal from chambers at the top as they are imaged at different times. The

difference in time between the top-left-most and bottom-right-most chambers is about 11 minutes, and the fluctuations in bulb intensity are in the order of less than a minute, accounting for differences in correlation between rows. Leaving the lamp on and letting it stabilize for hours before initiating an experiment can help minimize these fluctuations. However, despite being the largest source of noise, the fluctuations are about 10% in magnitude and therefore can be tolerated without correction for the purpose of the analyses described in this document.

Other less significant sources of noise exist as well, including imperfect segmentation of cell boundary, and subtleties arising from interplay between the narrow depth of focus, point spread function (PSF) and variable cell sizes (see supplementary information of Gordon et al. [62]). These are also negligible and not corrected for.

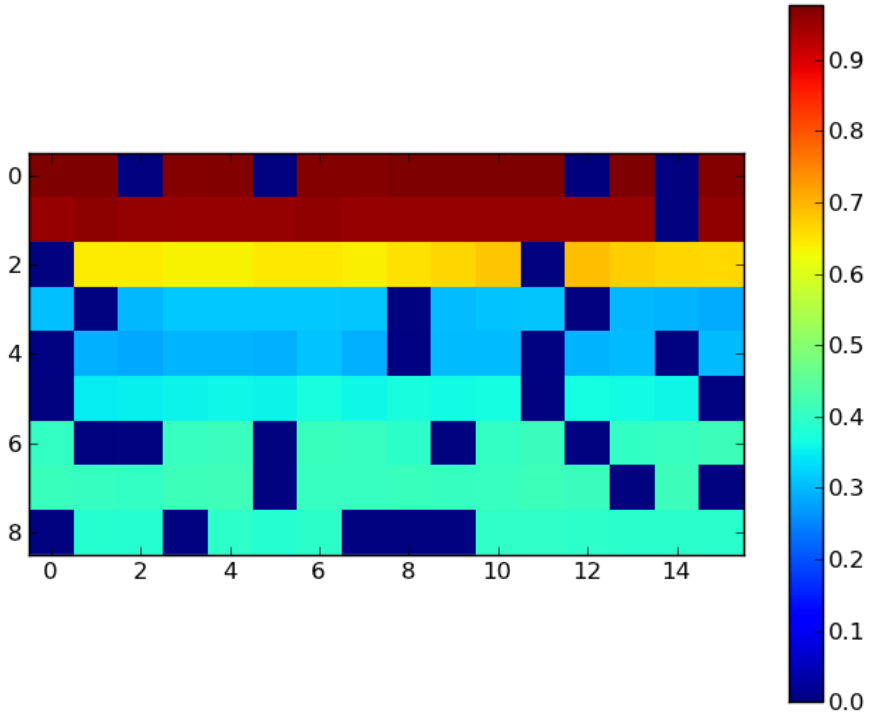

Figure 2-4 Fluctuations between mCherry and CFP signal are less correlated between distant chambers: The color indicates the correlation between the background mCherry signal in the 0^{th} row and 0^{th} column, against the background CFP signal in all other chambers. Since distant chambers are imaged farther apart in time, fluctuations in brightness between distant chambers are less correlated than chambers close to each other. This further supports that fluctuations from the excitation beam are the primary cause of variation in fluorescence measurements.

Chapter 3: Results

Synopsis

Here I show results derived from monitoring 8 different deletion strains of yeast cells under a transient pulse of pheromone and making quantitative single cell measurements of their transcriptional, arrest and morphological response while tracking the cells' lineages. I reveal knockouts with drastically different variability and heritability of signaling and using our lineage tracking capacity highlight mechanisms behind altered variability upon deletion of these pathway components. These mechanisms involve cell cycle regulation of MAPK and asymmetric cell division in yeast.

3.1 Single-cell screen of response to pheromone

The results from this chapter are all from experiments where after loading the cells onto the device, the cells are grown under rich media for the period of about 7.5 hours to track lineages, after which they are induced by 100nM pheromone for the period of 1 hour before the conditions are changed back to rich media for the remainder of the experiment (See Figure 3-1). The concentration of 100nM was chosen to be a concentration at which the cells are fully responsive according to dose-response curves shown in previously reported works [6,57] and also confirmed by our experiments (data not shown).

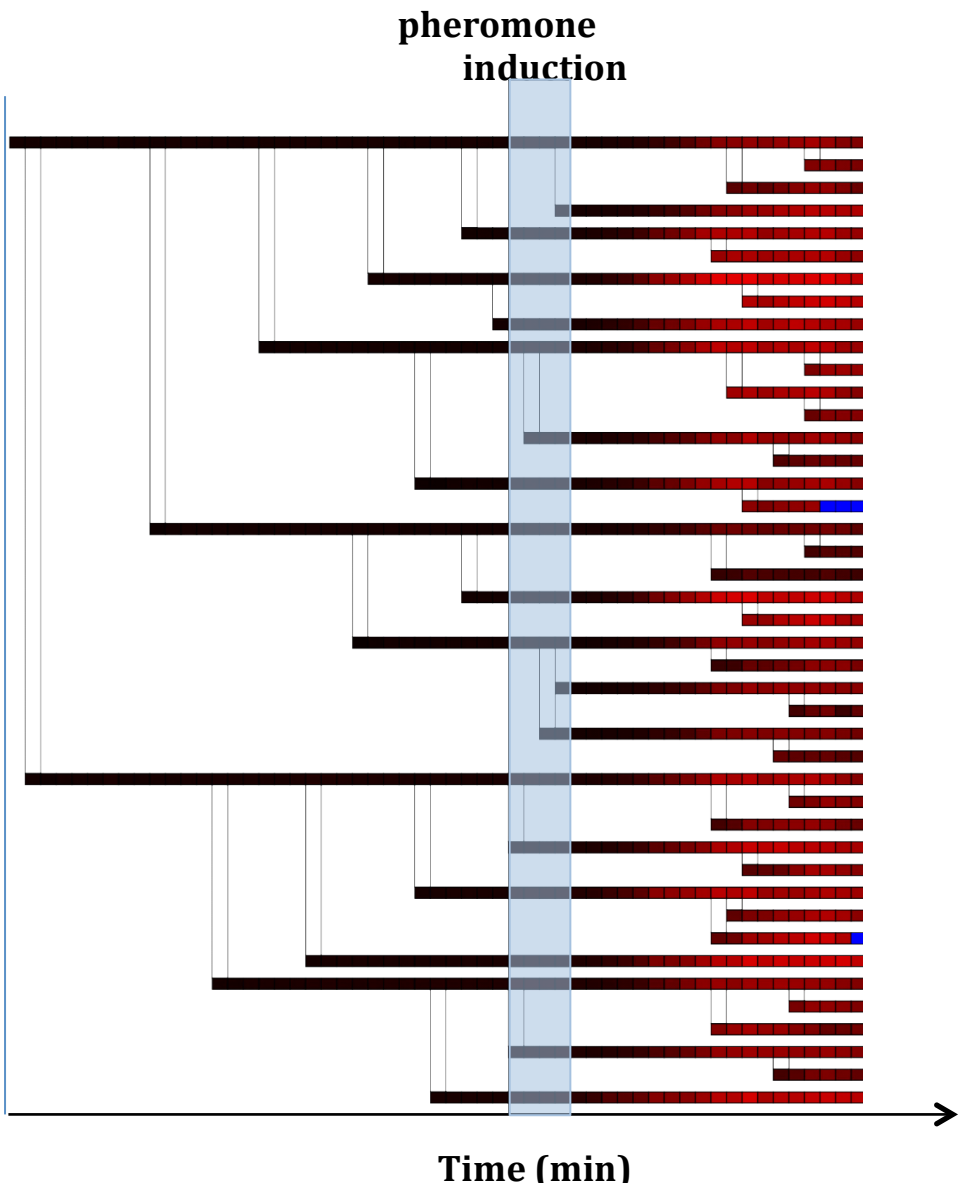

Figure 3-1 Experimental condition and sample tree: each horizontal line corresponds to a cell, where the position along the horizontal line indicates the time the cell was imaged and the color indicates the average mCherry fluorescence in that cell at that time point. Vertical white lines connect a daughters to their mothers also indicating the time of birth. The shaded region indicates when the cells were induced by pheromone, and during the remainder of the experiment the cells were constantly perfused with rich media.

Cell growth on the device was measured to be the same as off-chip with a doubling time of approximately 100 minutes (See Figure 3-2). The growth curves in Figure 3-2 also show that

WT cells transiently arrest upon induction before going back to regular growth after the removal of pheromone. In contrast, *Δfar1* cells, and to a lesser degree, *Δfus3* cells show reduced capacity to arrest. The comparison of growth rates of different strains will be discussed in more depth in the next section. An important technical point to mention is that consistent growth rates throughput the experiment was only achieved upon optimization of bovine serum albumin (BSA) concentration in the media from 1% to 0.1%. BSA is required to prevent alpha factor from sticking to channel walls, but too much BSA likely has the unintended effect of titrating nutrients *as well as* pheromone out of the solution, resulting in reduced growth rates. Indeed at 1% BSA it was observed that cell cycle periods would gradually get longer as growth was impeded (data not shown), while 0.1% BSA allowed for maintaining steady growth while also keeping pheromone in the solution.

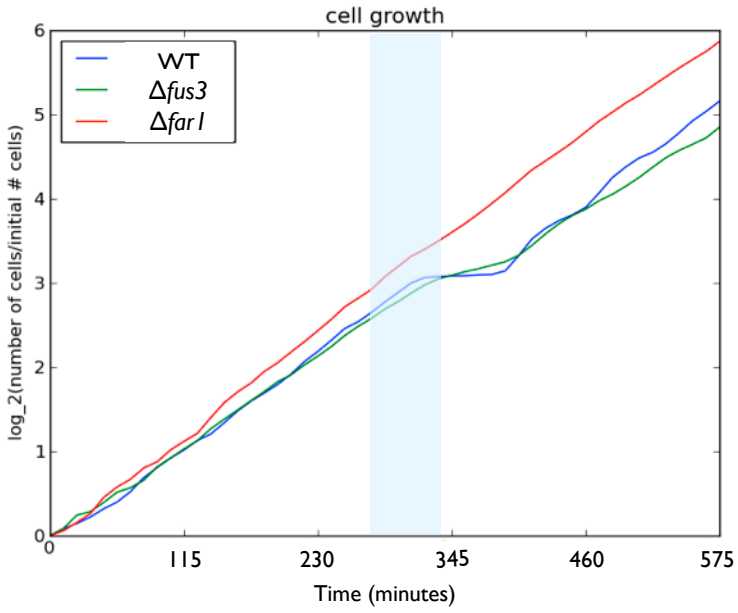

Figure 3-2 Growth curves for WT, *Δfus3* and *Δfar1*: Number of cells is normalized for initial cells and plotted on logarithmic scale against time. All strains show a linear trend as expected. The shaded region shows the transient alpha factor induction, which is followed by a temporary arrest by WT cells but not ***Δfar1***. The ***Δfus3*** mutant exhibits reduced arrest.

3.1.1 Transcriptional response

We measured the response of cells to pheromone stimulation by a mCherry fluorescent reporter placed under a PRE promoter (see Methods chapter for details). The mean fluorescence intensity in a cell was used as a measure of its signaling response capacity while the coefficient of variation in this quantity across the population as a whole was used as a measure of variability in response capacity (coefficient of variation = standard deviation divided by the mean). The comparison of mean response and variability in response for 8 different deletion strains are shown in Figure 3-3.

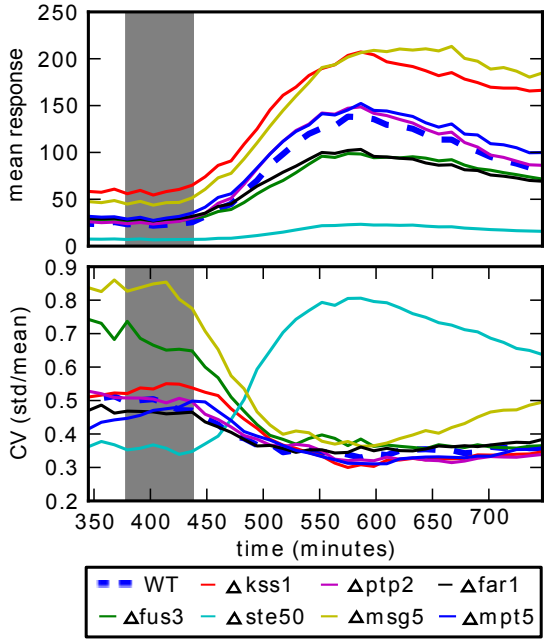

Figure 3-3 Mean and CV of mCherry response in all strains: Top – The average response of the population is presented as the mean response of all cells. Response of each cell is measured by the average pixel intensity in the mCherry channel. In line with previous reports, ***Δkss1*** and ***Δmsg5*** are hypersensitive, whereas ***Δste50***, ***Δfar1***, and ***Δfus3*** are less responsive than WT. Bottom – The cell-to-cell variability in response is measured by the coefficient of variation, which is calculated by dividing the standard deviation by the mean at every time point. All strains except ***Δste50*** show a decrease in CV, highlighting abnormally high variability in the ***Δste50*** mutant.

In agreement with previous observations, *Δmsg5* and *Δkss1* were found to be hypersensitive to pheromone whereas *Δfus3*, *Δfar1* and *Δste50* on average responded less than the wild type strain [1,3,57]. The distribution of response at t=540 minutes was found to be significantly different in all mutants as compared with WT (KS 2 sample test, p-value < 5e-4, pair-wise comparison). Interestingly the basal rate of expression (measured at t=350 minutes) in all mutants except *Δptp2* and *Δfus3* was also found to be different from WT (KS 2 sample test, p-value < 1e-8). This is most obvious for *Δste50*, ***Δkss1*** and ***Δmsg5***. In the case of ***Δkss1*** and ***Δmsg5***, the basal expression is increased compared to WT. This is in line with the reported functions of these two proteins: Msg5 is a phosphatase which dephosphorylates Fus3 and Kss1, the absence of which results in increased phosphorylated Fus3 proteins and hence higher transcription under PRE [7,31]; whereas Kss1 (in its inactivated form) is known for its inhibitory role on Ste12 activity [5,129]. In the case of *Δste50*, expression is reduced in both basal and activated states of the pathway (See Figure 3-4). The role of Ste50 as a facilitator of Ste11 phosphorylation near the membrane explains reduced response under pheromone stimulation. The reduced basal expression however is a more surprising aspect of the *Δste50* phenotype, since it suggests that even in the absence of pheromone, basal activity at the membrane is required and coupled to downstream activity in the nucleus.

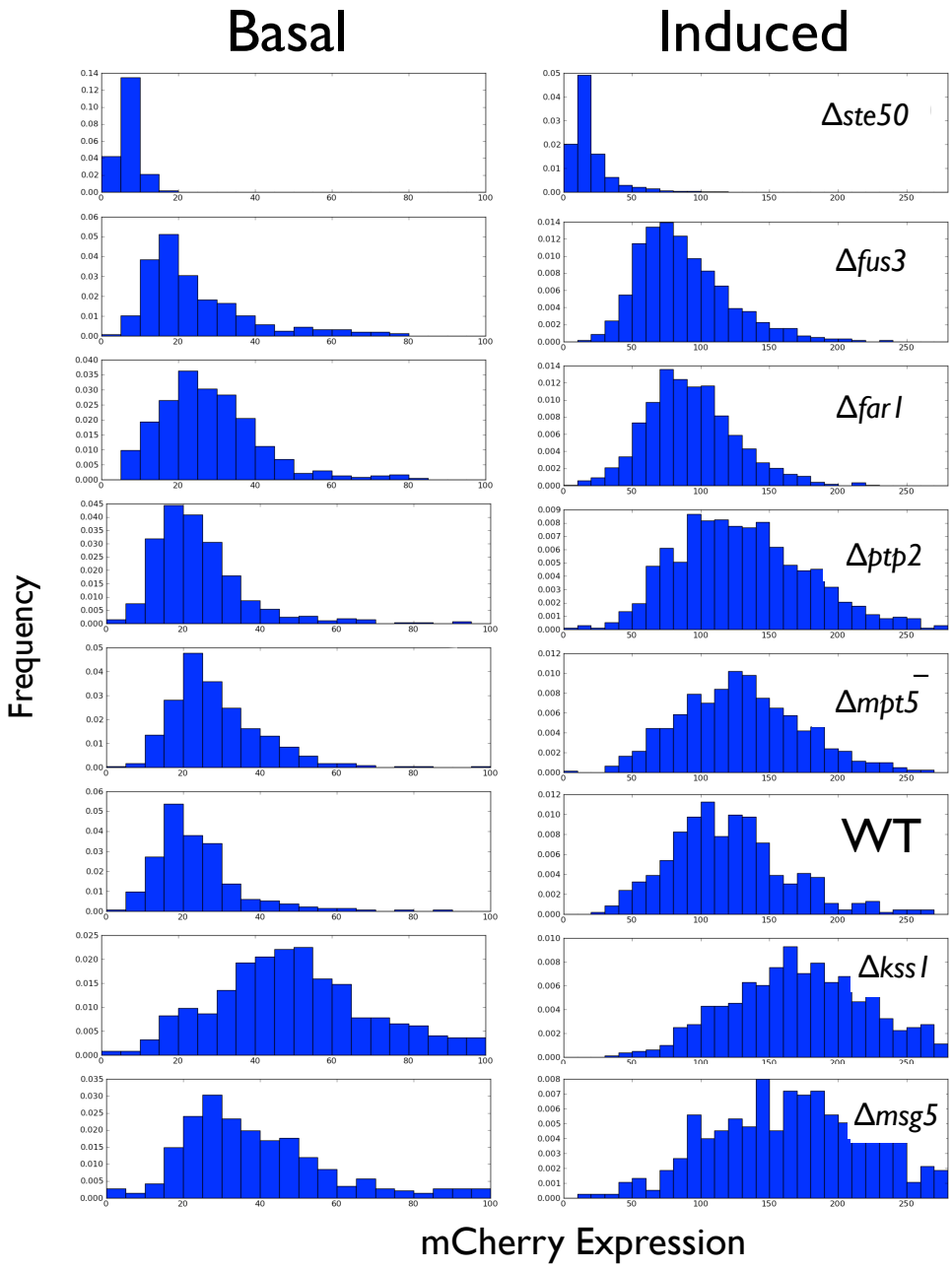

Figure 3-4 Distribution of mCherry expression in all strains under basal and induced conditions: High throughput Single cell resolution imaging allows for measuring response distribution of each population. Note that a small subpopulation of ***Δste50*** cells can respond as high as other non-sterile mutants such as ***Δfus3***, resulting in high CV in ***Δste50***.

Moreover, the single cell resolution of expression measurements allows for the calculation of variability in response across each population, which is shown in the bottom panel of Figure 3-3, where the coefficient of variation (CV) is used as a measurement of heterogeneity. The CV is defined as the standard deviation normalized by the average and is commonly used as a measure of variability, heterogeneity or "noise" [130]. While all strains show a similar decreasing trend of CV over time upon induction, *Δste50* stands out as the only mutant for which the variation increases relative to basal levels. As shown in the distribution of Figure 3-4, for *Δste50* and also in the time-course density plot of *Δste50* in Figure 3-5, for the majority of *Δste50* cells the fluorescence levels under pheromone are comparable to those at basal levels. Only a small subpopulation, appearing as a long tail in the distribution in Figure 3-4, show capacity to respond up to levels that match the response of other non-sterile mutants such as *Δfus3* and ***Δkss1***. The white lines in Figure 3-5 indicate trajectories of selected cells that demonstrate the wide range in response capacity in the *Δste50* and WT strains. It should be noted that, within the limitations of mCherry maturation times, we observe that it is the rate of expression that determines the overall responsiveness of the cells, and that the rise in signal occurs at about the same time point for all the cells (Figure 3-5, *Δste50*).

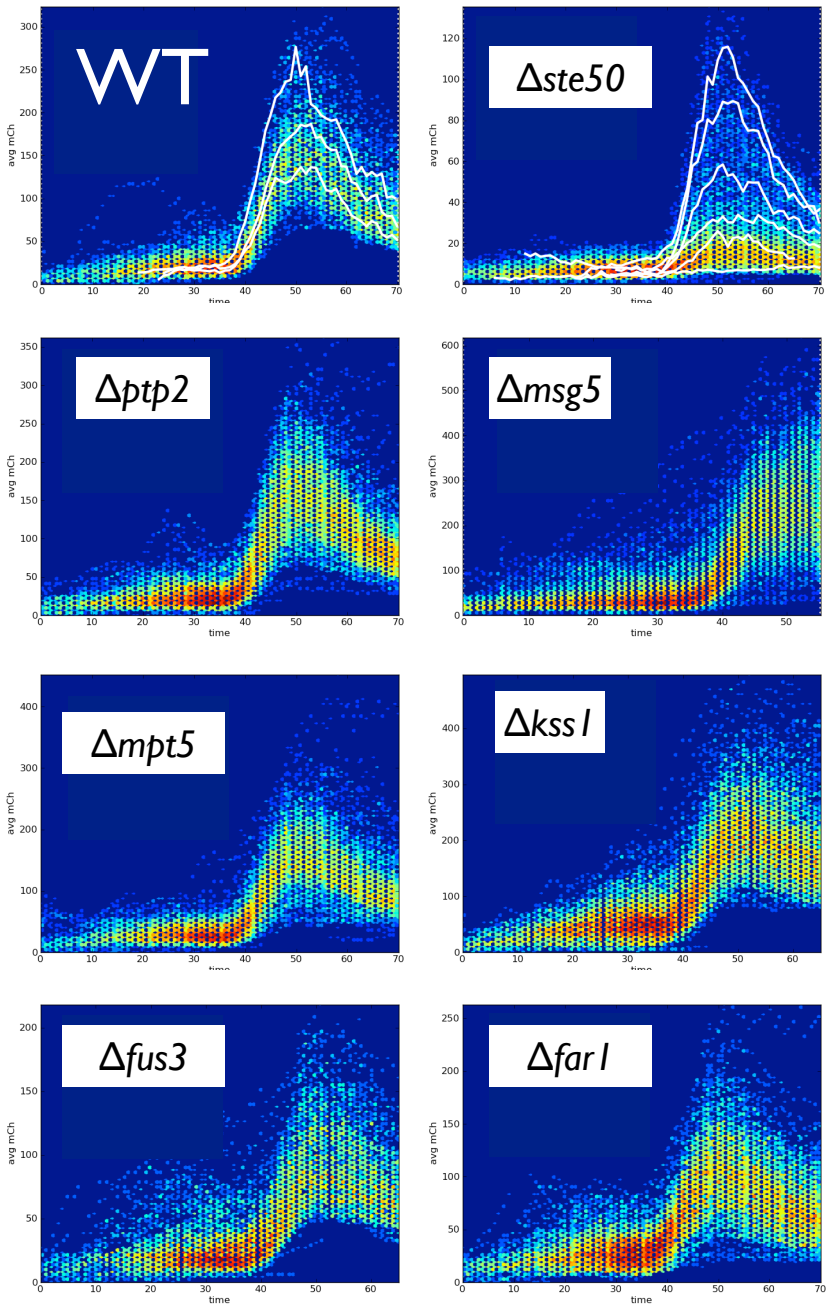

Figure 3-5 Single Cell trajectories of response: The density plots show the single cell trajectories of response of all cells in each population. The color indicates the number of cells at a particular response level at each time point. White lines in WT and ***Δste50*** show trajectories of select cells. While most ***Δste50*** cells do not respond, a small subpopulation exhibit sensitivity to pheromone.

3.1.2 Cell cycle arrest

While there are hundreds of genes which are transcriptionally altered upon pheromone induction [21], another major impact of pheromone on a cell is the halting of its regular cell cycle progression at START (see Introduction for details). While bulk measurements of cell growth can detect dramatic alterations to this arrest response (for example fully arresting vs. non-arresting cells), they cannot account for more subtle differences between strains in their ability to arrest their cell cycle upon pheromone induction. For example it has been proposed that FAR1-independent mechanisms of arrest exist [40] and several genes other than FAR1 were implicated; however, the limited sensitivity and throughput of conventional arrest assays make it difficult to screen different strains for alterations in arresting phenotype. There are two characteristics of our platform that address these problems: one is the capability to change the environmental conditions dynamically, and the second is the ability to measure cell cycle periods, with a resolution of approximately 11 minutes, using automated lineage tracking. The latter is made possible by simply noting the period of the time that is flanked by two buds off of the cell of interest. We exploited these features to develop an assay for arrest whereby a transient pulse of pheromone is applied to the cells, temporarily delaying their next division. This produces a more quantitative measurement of arrest capacity via quantification of the length of the stretched cell cycle period. Furthermore, this assay quantifies the arrest capacity at a single cell resolution unlike conventional methods. Figure 3-6 shows the measured distribution of periods under growth media as well as under pheromone stimulation for all 8 strains. Lineage tracking is used to distinguish between young cells and old cells which are known to have different periods [131].

There was no statistically significant difference between periods of old cells of any of the strains, with the exception of *Δfus3,* which had longer periods than any of the other strains. (p-value < 7e-3 KS 2 sample test). The periods of young cells weren't significantly different from one strain to another (all p-values of difference were above 1e-2). All mutants except *Δmpt5, Δ ptp2* and ***Δkss1*** were significantly different in the distribution of the arrested periods compared to WT (p-value < 8.8e-3). Most important to point out here is the distribution of arrested periods in *Δfar1*: cells lacking this component have a significantly reduced capacity to arrest, however it is also apparent from the distribution that a small subpopulation of cells can still arrest despite the absence of FAR1. This corroborates with previous speculations that FAR1-independent mechanisms of cell cycle arrest exist in the cell [40].

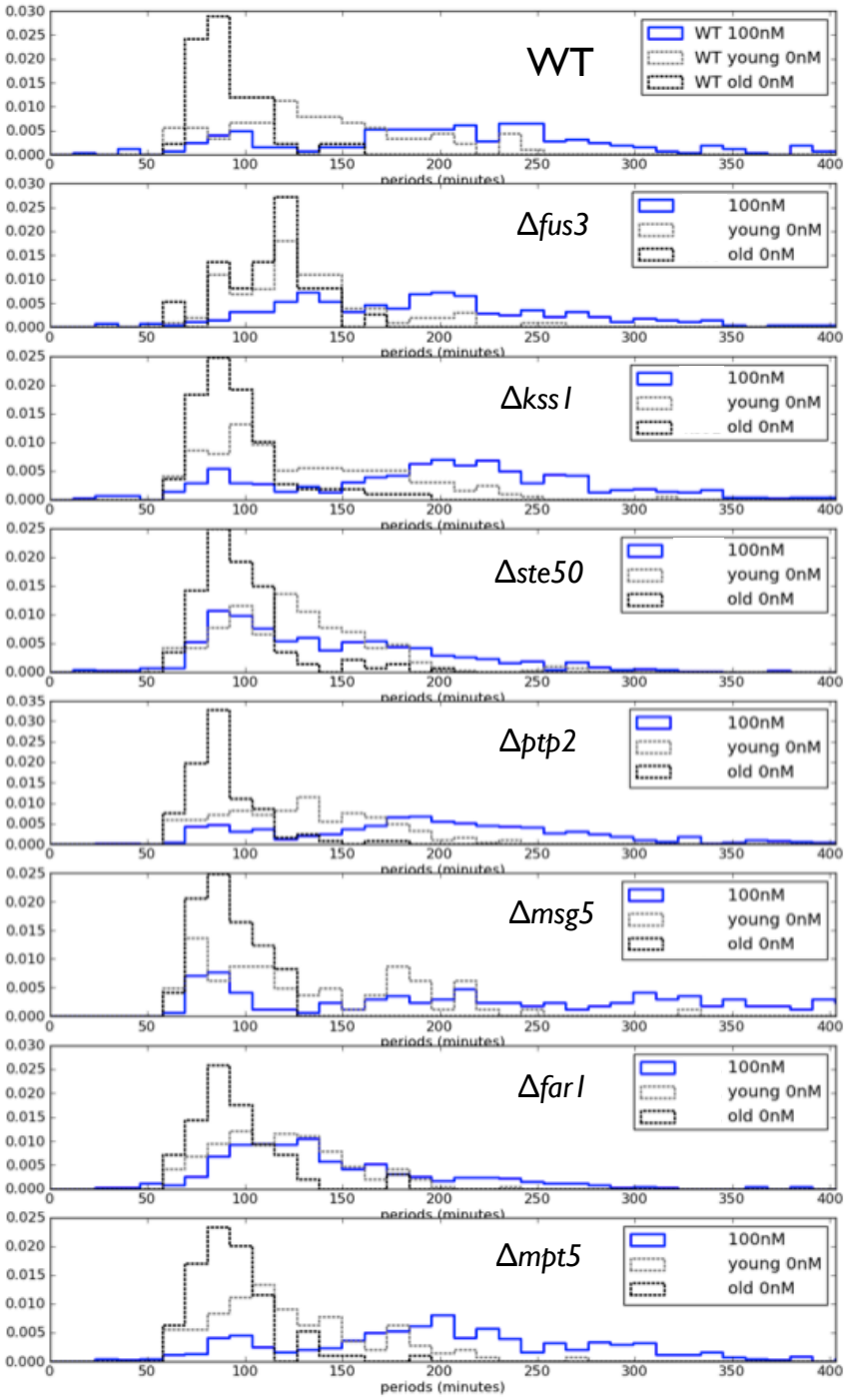

Figure 3-6 Cell cycle periods under media and induced conditions: Black and grey curves show distribution of periods of old and young cells, respectively, under regular growth conditions. Blue curves show distribution of periods of induced cells. Since the induction is transient, induced cells will recover after a stretched period and divide, allowing for a novel and quantitative measure of pheromone induced arrest.

3.1.3 Changes in morphology

Yeast modify their morphology in response to various stimuli or stresses. As already mentioned, in response to high concentrations of pheromone they form projections called "shmoo" formations, and at lower concentrations of pheromone they elongate in order to reach the opposite mating type which is presumed to be distant. In response to nutrient or nitrogen starvation, cells also exhibit a "foraging" phenotype which also involves elongated cell morphologies and 'invasive growth' into the surrounding medium. Furthermore, various mutations in the cell cycle network lead to larger or smaller than normal cell size yielding insight into growth mechanism and cell cycle control. It is therefore valuable to have access to single cell information about a cell's morphology and size.

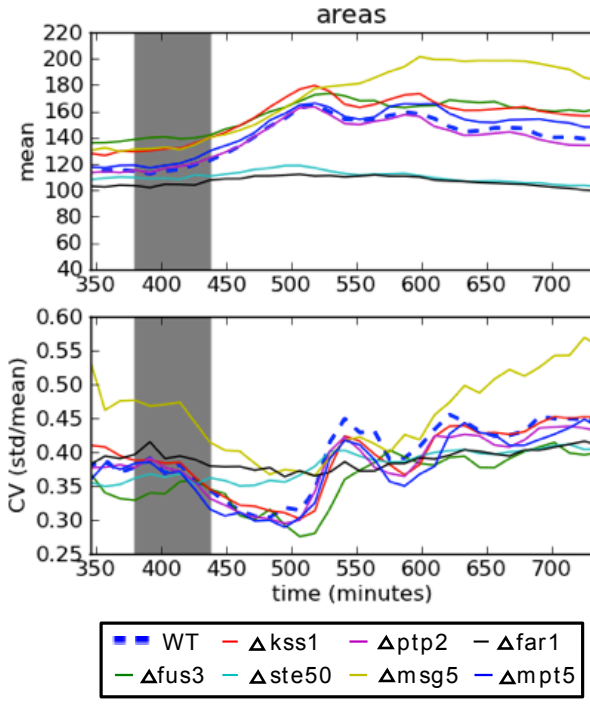

Figure 3-7 Cross-sectional area as a measure of morphology: Cell morphology changes in response to pheromone. Pathway components can influence cell size both in the absence and presence of pheromone. The oscillations in both mean and CV reflect synchronization of cells as explained in text. Deletions in pathway components affect cell size even in the absence of pheromone.

Here cross-sectional area of a cell is used as a morphological characteristic of the cells. The comparison of cell area in the 8 different strains is shown in Figure 3-7 and Figure 3-8. Figure 3-7 shows the mean and CV of cell size in the population during the course of the experiment. Even in the absence of pheromone it can be seen that the cell size is affected by deletion of pheromone pathway components. Whereas *Δfus3, Δkss1* and ***Δmsg5*** have a larger size, *Δfar1* and *Δste50* have smaller than WT cell size. While FAR1 overexpression has been shown to yield larger cell size, the phenotype in the other mutants has not been reported to our knowledge. It is important to note that alterations to cell size is not merely a result of alterations to signaling capacity of the pathway as both *Δfus3* and *Δfar1* have identical mCherry expression, but dramatically different sizes. The oscillations observed in mean and CV of cell size in the population reflect the synchronization of cell cycle and division upon pheromone induction: When buds are born in synchrony, the mean population size drops to its minimum as the CV increases to its peak. As is clear from Figure 3-7 and Figure 3-8, pheromone induction results in cell size increase. This is likely a product of cell cycle arrest, where cells remain in G1 and therefore continue to grow in the presence of pheromone. In agreement with this, *Δfar1* mutants (which do not arrest), do not show significant increase in cell size either. It is also interesting to note that after induction (Figure 3-8), the bud size, in accordance with the increase in size of the mother cells, also increases. This suggests there is a regulatory mechanism that maintains mother-bud size ratio at division. This observation also highlights the high resolution and sensitivity of the segmentation algorithm in detecting the moment of mother-bud separation.

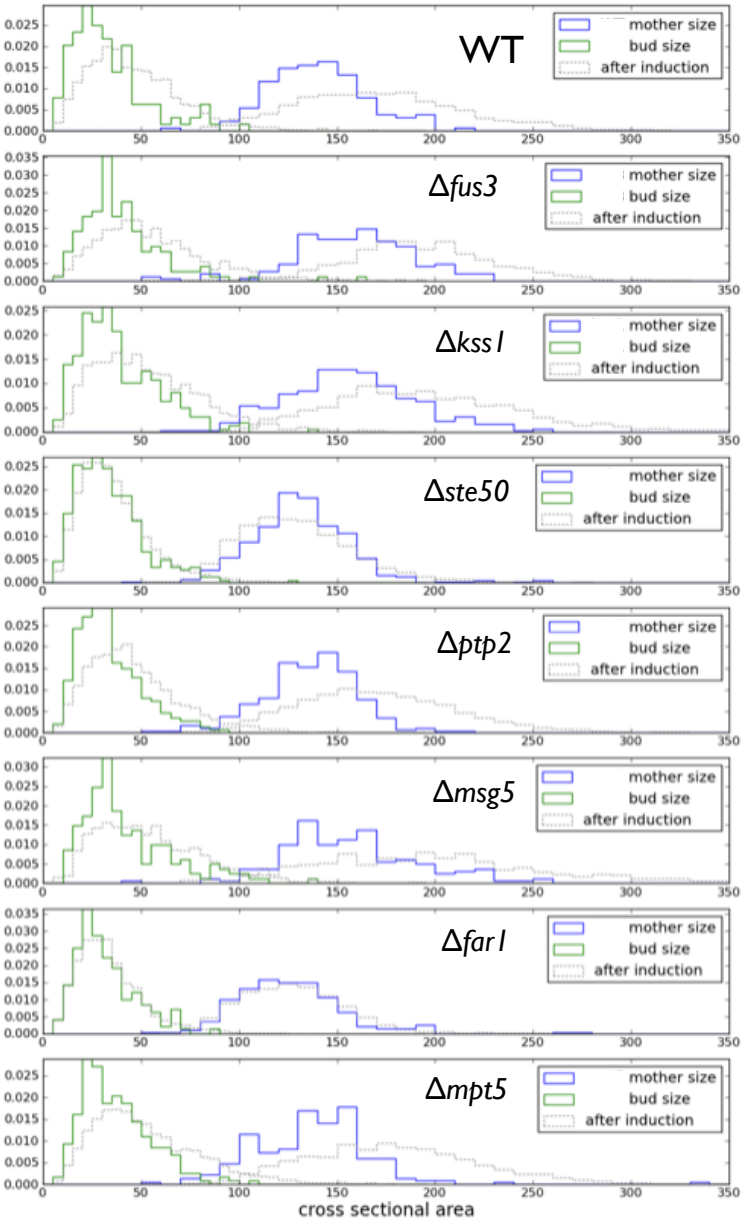

Figure 3-8 Distribution of bud size and mother size at birth: Green line shows the distribution of size of buds when they were first segmented and considered born. The blue curve shows the distribution of size of these buds' mothers at this time point. These distributions are for cells growing in rich media. The grey curves show how the green and blue distributions shift after pheromone induction, demonstrating that both mothers as well as buds increase in size upon signaling. The units of size are pixels in the image that are attributed to the cell by the segmentation algorithm.

These results were presented to demonstrate the capacity of the platform to acquire data on cell morphology. Even though morphology and pheromone pathway are closely related, the focus of this study is on transcriptional response and cell cycle coupling with the pheromone pathway. Therefore, the novel observations of abnormal cell morphology mentioned above were not pursued further.

3.2 Signaling capacity is non-genetically inherited

In the previous section I showed that variability in response is dependent on strain and that *Δste50* in particular exhibits unusually high levels of variability. In this section I address questions surrounding and the origins of this variability and quantify heritability of response capacity in the pheromone pathway.

To do this, we compared response of mother cells to those of their daughters. Mother-daughter (MD) pairs were chosen where the daughter was born before the induction of pheromone, and their response was measured 3 hours after the end of the pheromone pulse. Figure 3-9 shows the correlation of daughter response to those of their mothers as a density scatter plot. Two major points here should be highlighted: (1) *Δste50* exhibits an asymmetric scatter plot with daughters exhibiting higher capacity to respond. (2) Amongst the rest of the mutants, while the scatters are symmetric around the diagonal, the degree of correlation between the MD pairs appears to be different, with *Δfus3* exhibiting the highest levels of correlation.

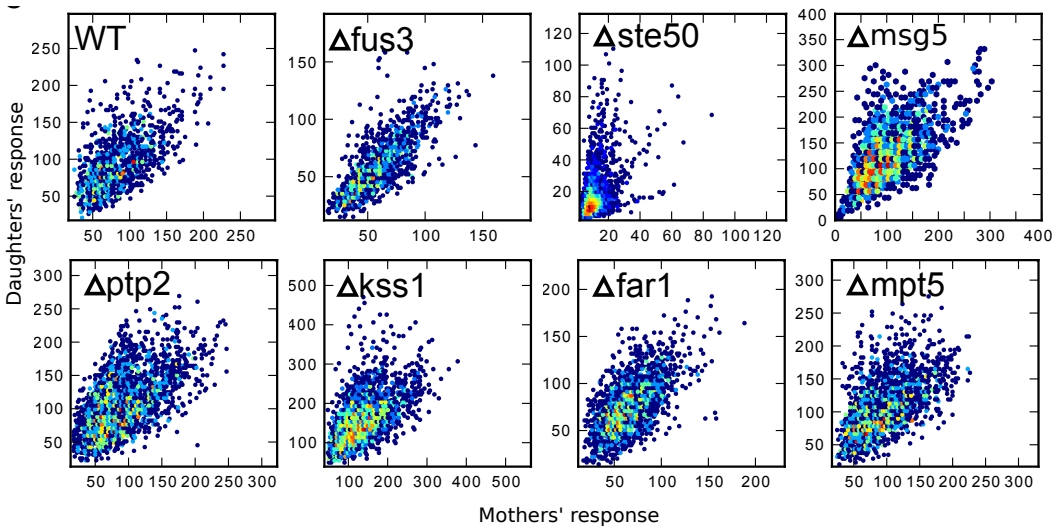

Figure 3-9 Comparison of mother-daughter pairs' response: The x-axis shows the response of mother cells and the y-axis shows the response of their respective daughters. These density scatter plots qualitatively demonstrate how different deletions in the pathways result in variations in degree of similarity between mother-daughter responses. The mutants ***Δfus3*** and ***Δste50***, stand out: Where mother-daughter pairs in ***Δfus3*** are very similar in response and symmetric around the diagonal. On the other hand, ***Δste50*** pairs exhibit asymmetry, where daughters appear more responsive than their mothers.

In *Δste50* the mean response of young cells, defined as cells that have never before being induced, is significantly larger than those of old cells, defined as those that have divided at least once before being induced (Figure 3-10) (KS 2 sample test, p-value = 8.23e-3). The error bars indicate the standard error of the mean. This data suggests that the enhanced heterogeneity in *Δste50* presented in Figure 3-3 is is linked to division processes and/or aging.

Figure 3-10 Comparison of response between young and old cells in *Δste50:* Cells with higher replicative age are less likely to respond in ***Δste50*** cells (KS 2 sample test, p-value = 8.23e-3).

For the rest of the strains that didn't exhibit such asymmetry we used the spearman (ranked) correlation coefficient to quantify the degree of heritability of response capacity. As seen in Figure 3-11, the correlation coefficients were different for each strain, quantitating the qualitative differences pointed out in Figure 3-9. In order to test whether these values are statistically significant we compared them to the correlation coefficient of an equal number of randomly selected pairs from the same population. This randomization was repeated one thousand times, and each time the correlation coefficient measured. The distribution of these correlation coefficients is shown in blue in Figure 3-11. Note that the randomization was performed separately for each strain, however since the distributions were the same, only one is shown in Figure 3-11 for visual clarity. The 95% confidence intervals (black bars) were calculated using Fisher's Z transformation [132] and a Z-test performed between MD and randomized pairs to measure significance of the difference: in all strains MD pairs were significantly (p-value < 0.01) more correlated than random pairs. These results show that a significant portion of the capacity to respond to pheromone is non-genetically inherited in

Yeast, an observation that parallels previously reported accounts of non-genetic heritability of cellular state in higher eukaryotes [63,118]. Comparison of strains against each other showed that *Δfus3*, *Δptp2,* and ***Δmsg5*** were statistically different from WT (p-value < 0.05), while *Δfus3* was significantly different from any of the other strains (p-value < 1e-4). The reduction in correlation in ***Δmsg5*** and *Δptp2* relative to WT can be associated with their roles as negative regulators of the pathway. It is well understood that negative feedback on a signaling cascade improves signal transmission by reducing the variability or "noise" in that system [6102]. It is therefore predictable that variability of the output of a signaling pathway will increase upon removing a negative regulator of the pathway, as is the case with *Δptp2,* and ***Δmsg5***. This increased variability is reflected in the average difference in response between MD pairs and therefore a reduction in the correlation coefficient. In the case of *Δfus3* however, the underlying mechanism is not as obvious since FUS3 is the main kinase in the pathway and responsible for phosphorylating many proteins of various functions. In the following section we use the lineage tracking capacity of our platform to measure cell cycle periods to address the specific regulatory role of FUS3 that may explain the increased heritability of *Δfus3* mutant.

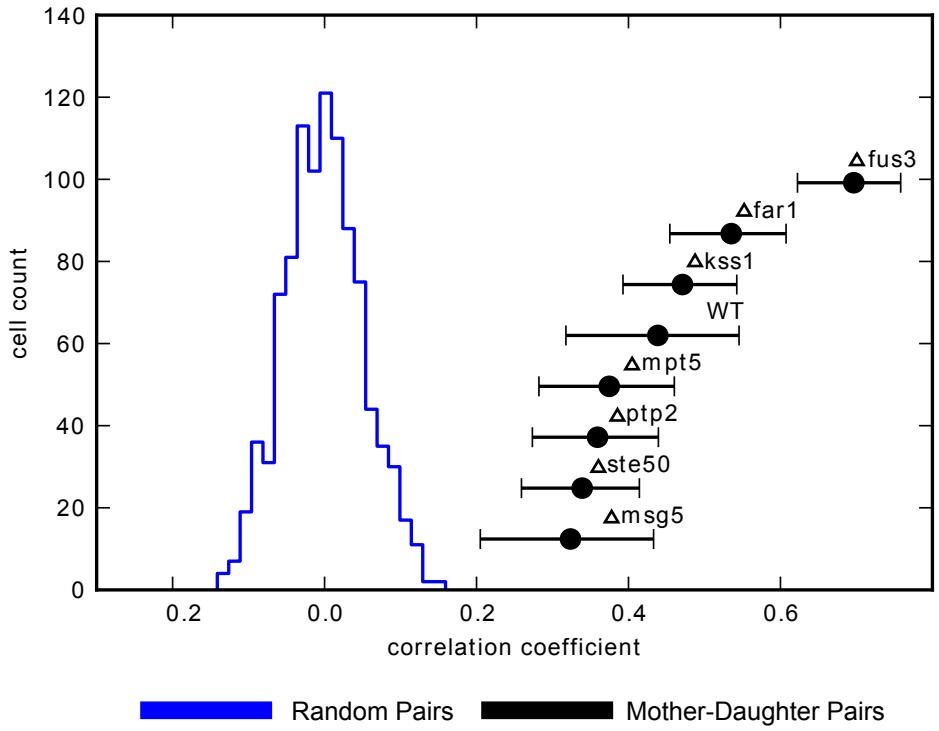

Figure 3-11 Comparison of response correlation in MD pairs of different strains: Quantification of the correlation between mother and daughter response for all strains shows that MD pairs in all strains (black) are significantly more correlated than those of random pairs within the population (blue). This implies that the capacity to respond to pheromone is non-genetically inherited. Furthermore, deletions in the pathway result in differences between the degrees of this correlation. Namely, ***Δfus3*** shows significant increase in heritability relative to all other strains.

3.3 Cell cycle as a source of variability in signaling capacity

It has previously been reported that cell cycle asynchrony accounts for about half of the variability observed in pheromone signaling [9]. This variability is associated with CDK28 inhibition of MAPK signaling after START (see Introduction) [44,46]. While previous works control for this variability by synchronizing the cells via chemical inhibition of the cell cycle [6,9,133] our platform allows for *in silico* synchronization of the cells during the regular course

of the cell cycle. This in turn facilitates the screening of various mutants for the role of the deleted protein in cell-cycle mediated MAPK suppression.

Suspecting that the increase in heritability in *Δfus3* may be linked to the cell-cycle influence, we compared the correlation coefficient of pairs that were induced at progressively longer time points into their cell cycle (See Figure 3-12). While WT pairs exhibited a drop in correlation as time passed on, *Δfus3* cells appear to maintain high correlation irrespective of the progression of the two cells further into the cell cycle. Note that for pairs that were induced immediately after the pair were born (i.e. the first data point on Figure 3-12), both WT and *Δfus3* show the same high degree of correlation. This observation suggests that heritability in the two strains is the same at division. However, in WT the progression of the cell cycle degrades this initial correlation, whereas *Δfus3* seems to be immune to this effect.

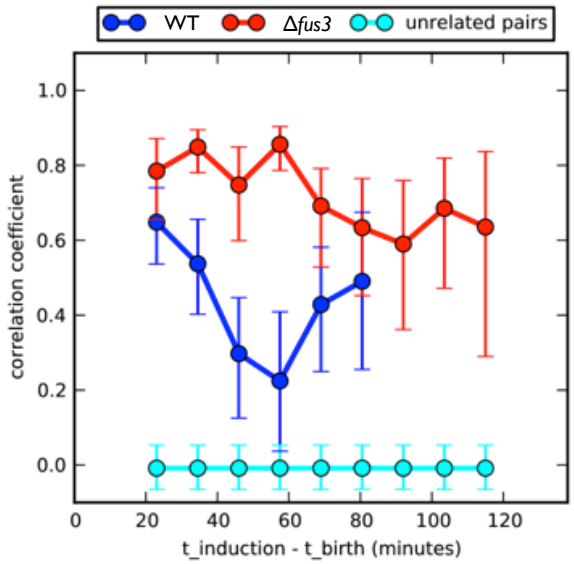

Figure 3-12 MD response correlation drops as the cell cycle progresses in WT (blue) while in *Δfus3* (red) it remains the same: This observation suggests that the high heritability of signaling capacity in ***Δfus3*** may be due to its immunity from de-correlative effects of cell cycle progression on signaling observed in WT. The cyan and green curves show the correlation of unrelated pairs as control. The error bars measure the 95% confidence interval from bootstrapping analysis.

As previously mentioned, the periods of old cells in the *Δfus3* population were significantly longer than any other strain screened, while for the young cells, periods were the same length in all strains. The same experiment was run on WT and *Δfus3* strains alone, producing more data points for the cell cycle measurements, summarized in Figure 3-13. Aside from longer periods of old cells under regular growth conditions, *Δfus3* periods also differ from WT under pheromone condition: while WT shows a bi-modal distribution, where some of the cells do not arrest and divide with regular periods; the *Δfus3* population is uni-modal and the non-arresting population less distinct from the arresting population as is the case in WT (p-value = 2.3e-6, KS 2 sample test).

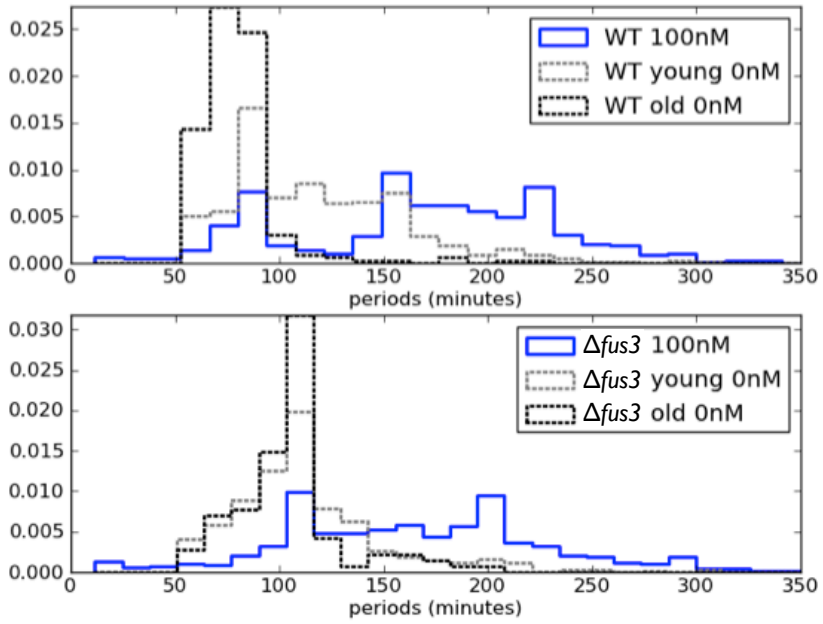

Figure 3-13 Comparison of WT and *Δfus3* periods under normal and induced conditions: As before, black and grey lines show the periods of old and young cells, respectively, under 0nM of pheromone while the blue curve shows the periods of cell cycles which experienced a transient pulse of 100nM pheromone. Comparison of black and grey lines between WT and ***Δfus3*** cells shows that old ***Δfus3*** cells appear to grow more slowly than in WT. Furthermore, comparison of blue curves between the two strains shows that WT cells exhibit a more pronounced bi-modality than ***Δfus3***.

Given that pheromone signaling is inhibited after START, we hypothesized that the non-arresting cells in WT must be those that are already committed to START and have initiated their S phase. In order to confirm this, we synchronized the cells "*in silico*" and measured response as a function of the cell phase. The cell phase was measured by the number of minutes the cells were into their cell cycle when induced. Figure 3-14 shows the median transcriptional response of cells as a function of their cell phase at the time of induction. It is clear that there is a transition about 50% of the way through the cell cycle in WT, where cells' response is inhibited. In comparison, *Δfus3* cells show a much more uniform level of response throughout the cell cycle.

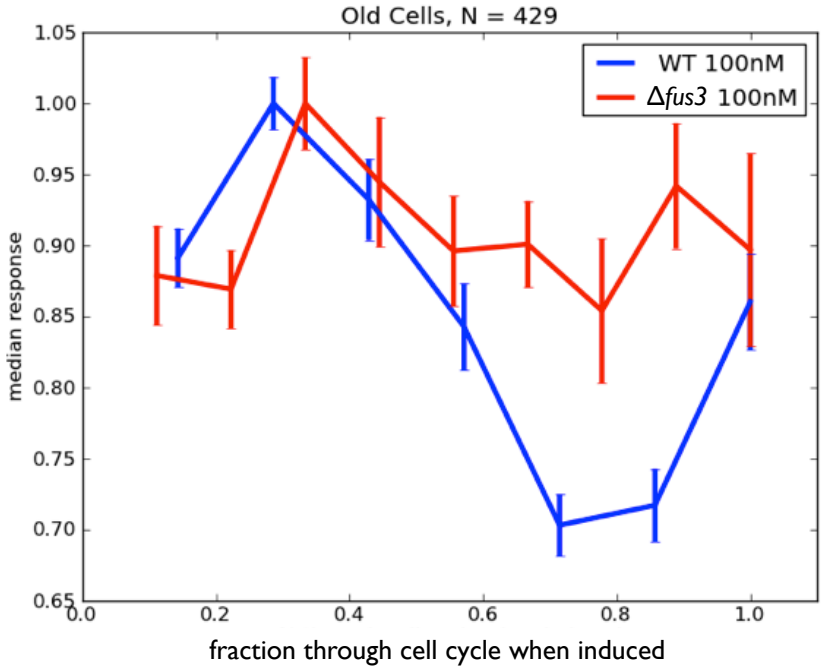

Figure 3-14 Response as a function of cell phase upon induction: Signaling is inhibited by the S phase and therefore a reduction in response is expected for cells that are induced later in their cell cycle. However, ***Δfus3*** cells show reduced inhibition of signaling during this latter phase of the cell cycle as compared to WT. Errors bars are standard error of mean at each point.

This reduced inhibition of the MAPK during S phase also manifests itself in the arresting phenotype of *Δfus3*. As shown in Figure 3-15, while WT cells fully arrest when induced in the first 50% of their cell cycle, they sufficiently suppress pheromone signaling to avoid arrest when committed to S phase. Unlike WT, *Δfus3* cells still arrest in S phase (although to a lesser extent than in G1) as their periods are longer compared to the average period in regular growth conditions (dashed lines). These observations account for the noted absence of the distinct bimodality of periods in *Δfus3* that was seen in WT (Figure 3-15, blue lines).

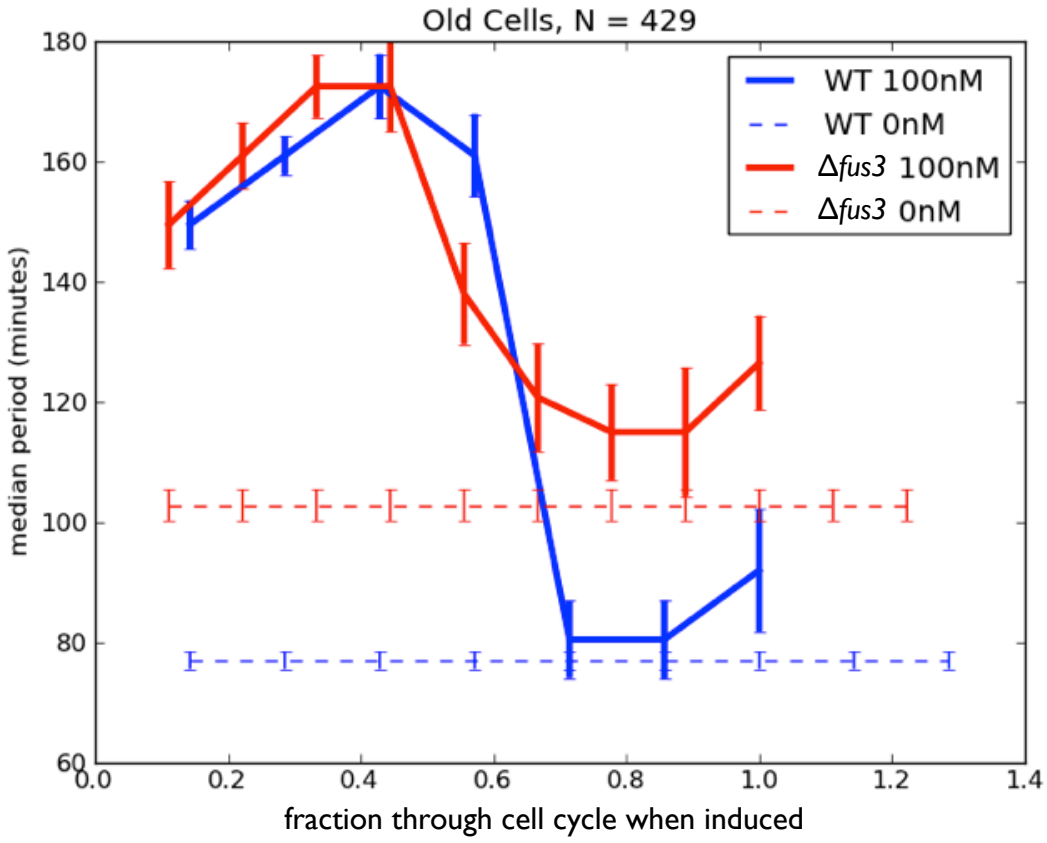

Figure 3-15 Cell cycle arrest as a function of cell phase upon induction: Signaling is inhibited by the S phase implying that arrest only occurs in cells induced in G1 phase (blue curve, WT). In ***Δfus3*** however, cells undergo moderate arrest, despite being in the S phase (red curve, >70% through the cell cycle.) The error bars signify the standard error of the mean.

The combination of data shown in Figure 3-13, Figure 3-14 and Figure 3-15 suggest that FUS3 promotes transition from G1 to S. In the absence of FUS3, this transition is weakened, resulting in longer periods in old cells that normally have a shorter G1 period compared to young cells (Figure 3-13). This impacts pheromone signaling, as it implies a weaker S phase and therefore a less pronounced inhibition of MAPK signaling which normally occurs in S phase (Figure 3-14). In the absence of adequate inhibition of MAPK in S phase, more *Δfus3* cells arrest in S phase as a consequence of MAPK signaling (Figure 3-15). Finally, the reduction in MAPK inhibition by the cell cycle in *Δfus3* cells results in the reduction of signaling variability which is imposed by the cell cycle in WT (Figure 3-12), explaining increased levels of heritability in *Δfus3* cells (Figure 3-11).

The main role of FUS3 in the context of cell-cycle regulation is thought to be phosphorylation and activation of Far1 and therefore the promotion of arrest upon pheromone induction [134]. However, potential for a parallel proliferative function of FUS3 has also been suggested in two previous studies [40,43] which are substantiated by our findings.

Chapter 4: Discussion

Synopsis

Results described above show not only that the capacity to respond is non-genetically inherited in yeast, but that the degree of this heritability is affected by the presence and activity of pathway components. In the absence of STE50 there is a dramatic de-correlation between the response of mothers and daughters, whereas in the absence of FUS3, the heritability is dramatically enhanced. Here I discuss in more detail what the underlying mechanisms pertaining to each of these two strains may be. Moreover, I will discuss how our data complement the existing framework for non-genetic mechanisms of inheritance in eukaryotes.

4.1 FUS3 and the cell-cycle regulation of MAPK pathway

The increase in correlation in *Δfus3* cells was linked to the cell cycle modulation of signaling. We found that in the absence of *FUS3,* even in normal growth conditions, the cell cycles of old cells were longer than in WT strain, making them similar to the periods of young cells (Figure 3-13). Furthermore, the inhibition of signaling by the cell cycle during S phase was attenuated in *Δfus3* (Figure 3-14, Figure 3-15). While Figure 3-14 and Figure 3-15 were attained by *in silico* synchronization of the cells, we confirmed these results by doing a chemical synchronization of the cells (using hydroxyl urea) prior to pheromone stimulation and got the same results (Figure 4-21).

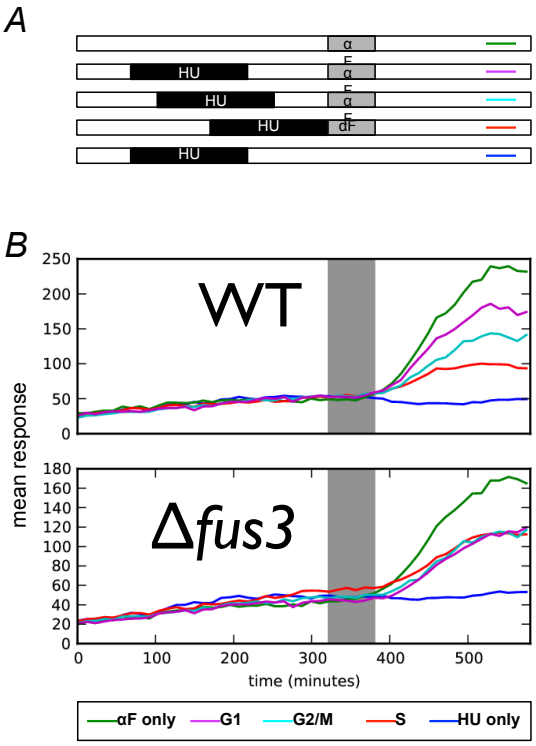

Figure 4-1 Chemical synchronization using Hydroxy Urea (HU): (A) HU results in arrest at S phase of the cell cycle. Schematic of 5 different experiments aimed to capture synchronized cells in different phases of the cell cycle when induced by alpha factor (αF). Induction took place at 0 (red), 58 (cyan), and 81 minutes (purple) after the end of HU treatment, roughly corresponding to S, G1, and G2/M phases of the cell cycle. (B) Confirming previous results from *in silico* synchronization of cells, WT cells show variability in response in different phases of the cell cycle, whereas *Δfus3* response is insensitive to the cell phase when induced.

Interestingly we only observed S phase inhibition of MAPK in old cells (i.e. cells that have divided at least once before induction). As is seen in Figure 4-2 young cells' transcriptional response does not appear to be significantly affected by the cell cycle. Consequently, in the absence of FUS3, the response vs. phase profile of old cells is very similar to that of the young cells. This similarity between young and old cells, which is a consequence of de-sensitization of old cells' signaling to cell cycle progression, manifests as more sustained

correlation between mothers and daughters and hence a high degree of heritability in MAPK signaling response. In comparing Figure 4-2 with Figure 3-154, it should be noted that the measurement of response over the course of growth of a young cell is influenced by the significant change in cell size that takes place in young cells. This is due to the fact that average mCherry intensity (corresponding to mCherry *concentration*) is used as our measure of response. Since the confounding effects of size affect the measurements in the earlier part of the cell cycle, the conclusions above should still hold as they concern relatively high levels of expression in the later part of the cell cycle, in S phase.

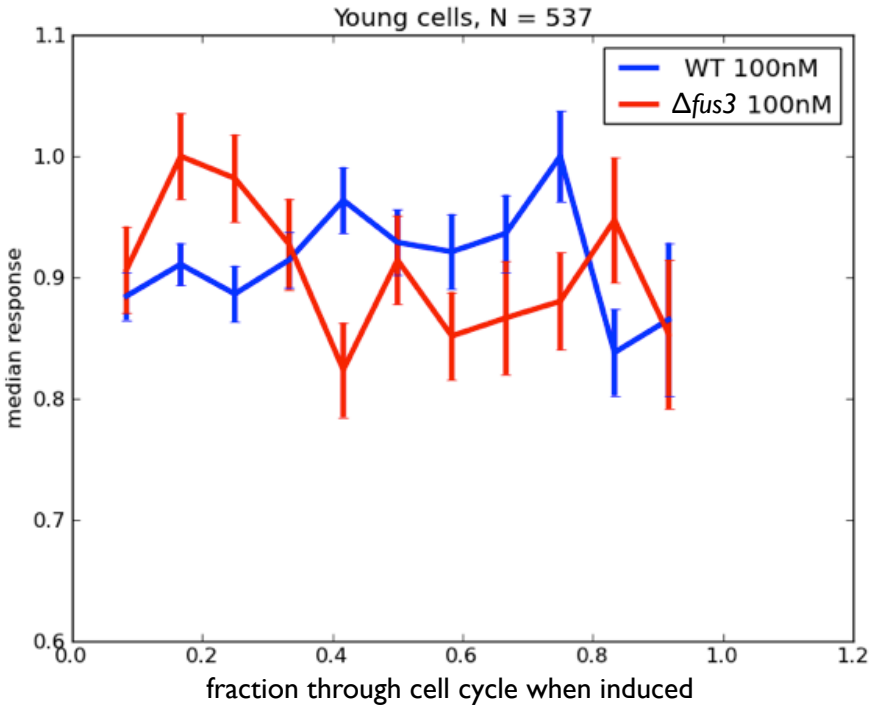

Figure 4-2 Response as a function of cell phase upon induction in young cells: Unlike old cells, young cells' response to pheromone is not as sensitive to cell phase at induction since the response inhibition in S phase is not observed in either WT or ***Δfus3***.

The increased cell cycle periods in regular growth conditions, and the reduced capacity of S phase to suppress pathway activity, point to a potential role of Fus3 protein in the promotion

and maintenance of the S phase. While this hypothesis contradicts evidence for the primary role of Fus3 as mediating the inhibition of START [86,134], it corroborates evidence for a parallel role of FUS3 as a positive regulator of the cell cycle [40,43]. In 1999, Cherkasova et al. suggest that Fus3p and Kss1p (i.e. active or phosphorylated forms of the species) on the one hand promote G1 arrest by inhibition of CLN1, CLN2 and CLB5 cyclins and on the other counteract G1 arrest by increasing CLN3 and PCL2 expression that promote budding. They propose that this proliferative function of Fus3 is to promote recovery from pheromone arrest. We showed that even in the absence of pheromone signaling deletion of FUS3 impacts regular cell cycle progression, specifically in old cells. In 2003, Cherkasova and colleagues demonstrated evidence for Fus3 involvement in proliferation [43]. However the mechanisms they suggested did not require Fus3p (in it's inactive form), and involved a coupling of the MAPK pathway with the Ras/cAMP pathway. They suggest that Fus3 (and Kss1) regulate cAMP levels, and that in their absence, cAMP levels rise and long-term survival deteriorates. The suggested mechanism of action is through regulation of Cdc25 by Fus3/Kss1, which is a guanine nucleotide exchange factor (GEF) for the Ras protein. Our data suggests that cell cycle progression is only slowed in the old cells, which provides insight into why only long-term survival is affected.

4.2 Asymmetric division in yeast and response asymmetry in *Δste50*

In *Δste50* we observed dramatic heterogeneity in the population that has previously been unreported. While most cells do not respond to pheromone, a small population of cells responds as highly as other non-sterile mutants like *Δfus3* (Figure 3-5). The comparison of response of MD pairs points to the division event and replicative age as the source of this

heterogeneity (Figure 3-9 and Figure 3-10). Furthermore, neither a longer stimulation nor stimulation with 2 consecutive pulses (with a rest in between) increased response in the old population. While revealing the mechanism of this asymmetry is not within the scope of our current data we speculate on two mechanisms that could account for the *Δste50* phenotype: (1) the inherent asymmetry in cell cycle progression between mothers and daughters, or (2) the inherent asymmetry in the distribution of pathway molecules at division.

The cell cycle inhibits signaling through disruption of the localization of Ste5 at the plasma membrane [46]. Ste5 is a scaffold protein that brings Ste11 (the first of the 3 MAPK's) to the membrane to be phosphorylated by Ste20 [3], while Ste50 promotes affinity between Ste11 and Ste20 [135]. Furthermore, it has been proposed that the delayed G1-phase in daughters is maintained due to repression of *CLN3* expression by daughter-specific factors Ace2 and Ash1 [84,136]. Thus, reduced CDK activity in young cells may lead to lower cell cycle inhibition of the pheromone signaling. The consequence of this for *Δste50* cells that already have a dramatically reduced Ste11 connectivity to Ste20 may be that only some young cells manage to establish connection at the membrane and initiate the cascade. What sets these few responsive cells apart from the majority of young cells that do not respond is not clear. The up-regulation of Ste11 or Ste20 have been shown to rescue the *Δste50* phenotype [135,137]. It is possible that stochastic variability in the numbers of these molecules accounts for why certain *Δste50* cells respond while others don't. This hypothesis is supported by the observation that cells with longer periods right before induction had a higher likelihood of response (see Figure 4-3). The reasoning is that these cells would have had more time to grow their pool of Ste11 or Ste20 via basal production and would therefore be more likely to respond.

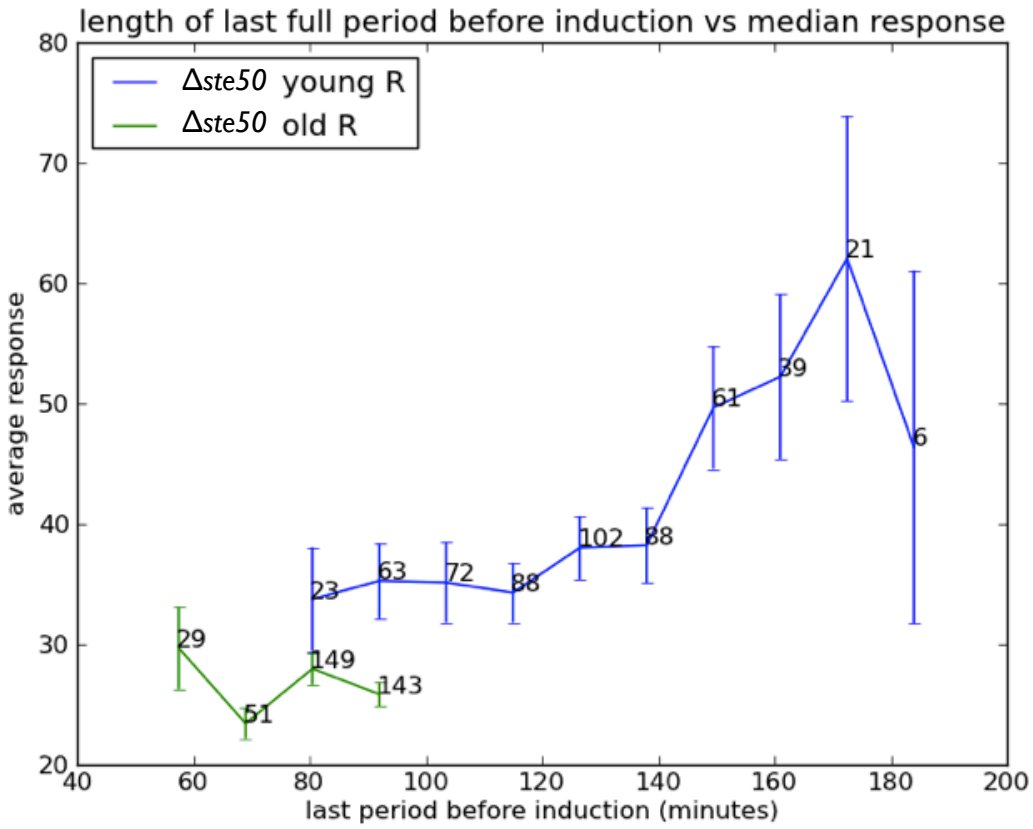

Figure 4-3 The length of the last period before induction influences response: Most ***Δste50*** cells do not respond to pheromone, irrespective of their replicative age. However, cells with a long cell cycle preceding induction, have a higher chance of response (blue curve). Error bars signify standard error of the mean and the numbers indicate sample size at each point.

Alternatively, there is considerable evidence in the literature for asymmetric segregation of molecules with a bias towards daughter cells. For example the protein Cdc42, which is positioned upstream of Ste50 in the membrane and is implicated in facilitating Ste20 phosphorylation [135,138], has been shown to be asymmetrically segregated towards the shmoo tip and the bud site during division [139]. Also, Geyer et al. reported that Cbk1, a protein kinase that controls daughter-specific production of several proteins, is functionally restricted to daughter cells and interacts with pheromone pathway proteins Ste5 and Ste50 [140-143].

It is important to note that cell cycle effects and asymmetric segregation of molecules are not necessarily independent processes and that one may affect the other. For instance, daughter-specific localization of transcription factors result in longer G1-phase in daughters compared to mothers as mentioned earlier [84,136]. In another example, Gehlen et al. showed that a delay in G2/M transition increased plasmid segregation into daughters at division which would be otherwise restricted and asymmetric due to nucleus geometry [144].

4.3 Stochastic expression and heritability

We showed cell cycle regulation of MAPK and asymmetric division to be important contributors to heritability of signaling and variability in signaling at large. Much effort has gone into understanding of non-genetic variability from stochastic gene expression as reviewed in the introductory chapter. While our methodology did not include dual-reporter assays used in many of these studies [60], aspects of our data address such questions. For example, mutants ***Δmsg5*** and *Δptp2* showed significantly lower correlation between mothers and daughters (Figure 3-11), and exhibited higher variability than WT at the population level in both pre-induction (basal) and post induction (activated) states (Figure 3-3). Given the role of both these proteins as a negative regulator of the pathway, these results echo the well-known influence of negative feedback as an attenuator of stochastic noise [102]. Reduction in heritability in these strains may therefore be attributed to increased stochastic variability in signaling and expression that act to "scramble" any inherited similarities between two related cells.

While intrinsic noise has been shown to act at time-scales much shorter than a single cell cycle [113], extrinsic variation was found to have time-scales that are larger than a cell cycle. As a result of this, extrinsic variability amongst a population can be inherited during division,

accounting for heritability seen in heterogeneous populations like in our data, or two other previous reports [63,118]. Both of these studies, one on the GAL4 network in yeast and the other on TRAIL signaling in Hela cells, have argued that stochastic transcriptional bursts account for the gradual loss of heritability over multiple generations. Indeed our data also capture the reduction in correlation in response between cell pairs, as the genealogical distance between them grows larger (Figure 4-4). Recent suggestion that stochastic division of molecules can account for observed variability in the population provide an alternative mechanism to the stochastic bursting hypothesis [112,114]. More detailed experimental observations are therefore needed to clarify the relative contribution of each of these possible mechanisms. While single molecule, dynamic, live cell imaging has been proposed as the experimental solution to this issue [112], there might be potential for our platform to address the problem through indirect means as discussed below.

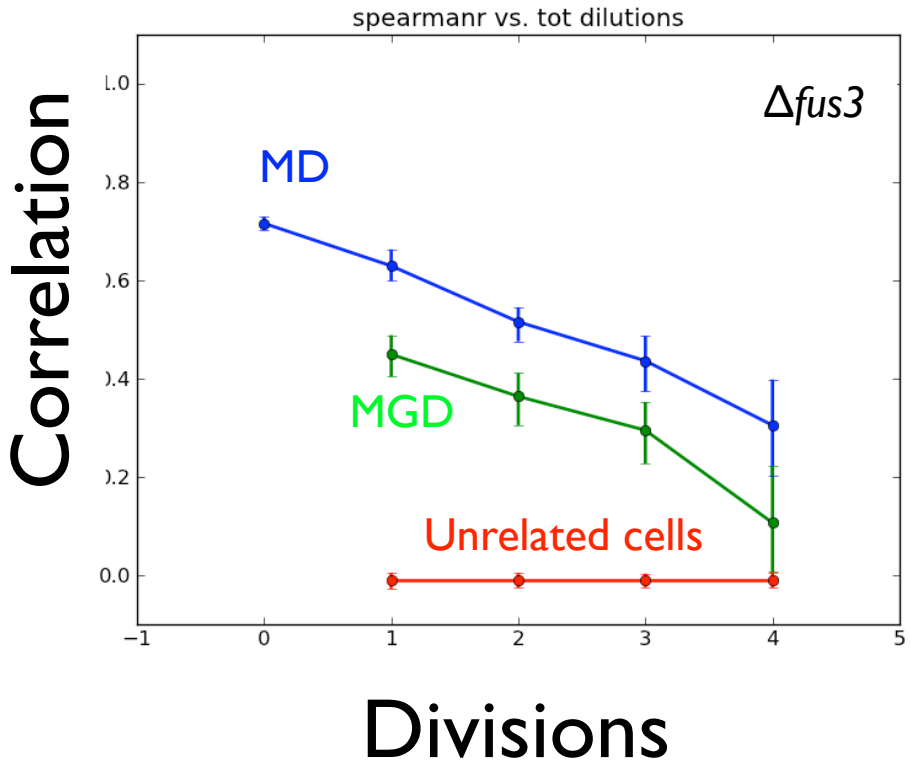

Figure 4-4 Correlation drops as genealogical distance grows: The correlation between mother-daughter (MD) and mother-grand daughter (MGD) pairs drops linearly with every division in either the ancestor or the descendant (x-axis) prior to induction. This is in line with a model where each division introduces some stochastic variability to a cell. The data is only shown for ***Δfus3*** where cell cycle effects are minimal. Error bars signify standard deviation of distribution of correlation coefficients resulting from bootstrapping.

Figure 4-4 shows how the correlation between cell pairs drops as the genealogical distance between them grows. Note that this data is only shown for *Δfus3* in which cell cycle effects are minimal compared to other strains and hence the decay in correlation is expected to be mainly from stochastic sources. The x-axis indicates the number of divisions either the ancestor or the descendent cell underwent before induction and the error bars indicate one standard deviation of the distribution of correlation coefficients derived from bootstrapping.

It is important to note that the stochastic segregation of molecules at division alone cannot account for our observations: In the event that stochastic division of molecules is the primary source of variability in a cell population, the correlation between a mother cell and it's daughter would have to be negative. Our data clearly show a positive correlation coefficient between mother-daughter pairs. Despite this, the act of division could be indirectly responsible for the correlation decay: each division involves the dilution of cellular components between the mother and the newly formed bud; this reduction in molecular numbers needs to be reverted during cell growth to replenish the levels of each molecule to the required concentration. Since expression is an inherently noisy process, this could account for reduced correlation with every division.

The linear drop in correlation coefficient (Figure 4-4) is consistent with this simple model. Moreover, the data suggests that when a mother cell undergoes replenishment of its components to recover from diluting effects of a division, its impact on the MD correlation is not as significant as when a bud replenishes after being born. This can be seen by comparing the slope of each line on Figure 4-4 to the distance separating the MD and MGD lines (blue and green respectively). While in the MGD pairs, two buds have had to replenish themselves after being born, in the MD pairs only one bud was required to do so. Therefore the distance between the two lines quantifies the effect of a single bud growth on de-correlation. The slope of each line on the other hand, quantitates the drop in correlation as a result of a mother cell undergoing growth/replenishment. The distance between the two lines is about twice as large as the slope of the two lines. This difference could be indicative of the larger growth a bud needs to undergo relative to a mother cell. The longer time spent in G1, and the larger

increase in volume could result in a more significant perturbation to the initial concentration than that experienced by a mother cell.

In light of these observations, the stochastic synthesis models proposed by others before [63,118] could be elaborated to link stochastic expression with cell cycle progression and cell growth. However, to experimentally support such a model would require a control condition where cell division is blocked, in order to evaluate whether a dilution at division is necessary for de-correlation or whether chronological aging alone can account for the de-correlation.

In summary, our results suggest that aside from cell cycle regulation of the pathway and asymmetric division of molecules at division, even stochastic synthesis may be directed and influenced by the division process, affecting non-genetic heritability in cells. This complements the existing models by recognizing that synthesis in mothers and daughters may occur to different extents and therefore affect each cells' "memory" of it's state in previous generations differently.

4.4 Conclusion

We have combined large scale microfluidics and time-lapse microscopy with automated image analysis to develop a unique platform that enables high-throughput lineage tracking and single cell measurements of multiple *S. cerevisiae* strains. With 128 experimental chambers in one device our system allows the tracking of thousands of cells and their lineages across 8 different strains exposed to up to 16 different conditions that are mixed from up to 8 chemical solutions [1]. Moreover, integration of robust high resolution microscopy makes our platform suitable for studying dynamic changes in protein concentration and subcellular localization across generations [58]. In addition to generating

single cell data on gene expression and genealogical relationships we can also retrieve quantitative information on cell cycle periods and chronological and replicative age. The combination of all these features allows for addressing biological questions that were not tractable using previously reported platforms[57,86,145,146].

We have applied this lineage tracking technology to investigate sources of cell-to-cell variability of the mating response in cell cycle and cell history. We have measured pathway activity upon pheromone exposure in thousands of cells and showed that responses of mothers and daughters were more correlated than responses between randomly chosen cells in all strains suggesting that the response capacity is non-genetically inherited by the next generation Figure 3-11. Moreover we showed that deletions in the pheromone pathway modulate the degree of this inheritance. On the one hand *Δfus3* exhibits heightened heritability of response capacity relative to WT and all other strains, while on the other hand, *Δste50* shows dramatic un-correlated asymmetry between the mothers' and daughters' response where daughter cells show superior capacity to respond compared to their mothers. The source of heterogeneity in monoclonal populations has been subject to heavy investigation. Stochastic gene expression [116,147,148] and more recently stochastic segregation of molecules at division [112,114] have been used to provide quantitative models of this phenomena. There has been less emphasis on studying the role of cell cycle on cell-to-cell variability despite reports that the cell cycle accounts for about half of the variability in the mating response [9]. We've shown that deletions in the pathway can impact cell-to-cell variability indirectly through modifying the coupling of the signaling network with that of the cell cycle and either increasing or decreasing the pathway sensitivity to pre-existing variability between the cell cycle states in the population. Furthermore, we observe that the

removal of Ptp2 and Msg5, which are two phosphatases that are activated by Fus3 and therefore act as a negative feedback loop in the pathway, increase variability between MD pairs (Figure 3-11) making them less correlated than WT and other strains.

There are practical implications of understanding the source of variability in signaling [118,122]. These range from applications in synthetic biological circuits to heterogeneity in pathological populations where noise is often desired to be minimized in order to achieve higher predictability or perhaps improved response to a drug [118]. As the pheromone pathway is a highly homologous prototype for many MAPK signaling pathways in higher organisms including humans, our results may implicate future strategies for targeting these pathways for therapy [149].

Bibliography

1. Falconnet, D. *et al.* High-throughput tracking of single yeast cells in a microfluidic imaging matrix. *Lab Chip* **11**, 466–473 (2011).
2. Qi, M. & Elion, E. A. MAP kinase pathways. *J. Cell. Sci.* **118**, 3569–3572 (2005).
3. Bardwell, L. A walk-through of the yeast mating pheromone response pathway. *Peptides* **26**, 339–350 (2005).
4. Hao, N. *et al.* Regulation of cell signaling dynamics by the protein kinase-scaffold Ste5. *Mol Cell* **30**, 649–656 (2008).
5. Paliwal, S. *et al.* MAPK-mediated bimodal gene expression and adaptive gradient sensing in yeast. *Nature* **446**, 46–51 (2007).
6. Yu, R. C. *et al.* Negative feedback that improves information transmission in yeast signalling. *Nature* **456**, 755–761 (2008).
7. Zhan, X. L., Deschenes, R. J. & Guan, K. L. Differential regulation of FUS3 MAP kinase by tyrosine-specific phosphatases PTP2/PTP3 and dual-specificity phosphatase MSG5 in Saccharomyces cerevisiae. *Genes Dev* **11**, 1690–1702 (1997).
8. Patterson, J. C., Klimenko, E. S. & Thorner, J. Single-Cell Analysis Reveals That Insulation Maintains Signaling Specificity Between Two Yeast MAPK Pathways with Common Components. *Science Signaling* **3**, ra75–ra75 (2010).
9. Colman-Lerner, A. *et al.* Regulated cell-to-cell variation in a cell-fate decision system. *Nat. Cell Biol.* **437**, 699–706 (2005).
10. Cookson, S., Ostroff, N., Pang, W. L., Volfson, D. & Hasty, J. Monitoring dynamics of single-cell gene expression over multiple cell cycles. *Mol Syst Biol* **1**, E1–E6 (2005).
11. Dohlman, H. G proteins and pheromone signaling. *Annual review of physiology* (2002).
12. Butty, A. The Role of Far1p in Linking the Heterotrimeric G Protein to Polarity Establishment Proteins During Yeast Mating. *Science* **282**, 1511–1516 (1998).
13. Nern, A. A Cdc24p-Far1p-Gbeta gamma Protein Complex Required for Yeast Orientation during Mating. *J Cell Biol* **144**, 1187–1202 (1999).
14. Johnson, L. & Lewis, R. Structural basis for control by phosphorylation. *Chemical Reviews-Columbus* (2001).
15. Soderling, T. R. Protein kinases. Regulation by autoinhibitory domains. *J. Biol. Chem.* **265**, 1823–1826 (1990).
16. Adams, J. A. Activation Loop Phosphorylation and Catalysis in Protein Kinases: Is There Functional Evidence for the Autoinhibitor Model? †. *Biochemistry* **42**, 601–607 (2003).
17. Lew, J. MAP Kinases and CDKs: Kinetic Basis for Catalytic Activation. *Biochemistry* **42**, 849–856 (2003).
18. Jansen, G., Bühring, F., Hollenberg, C. P. & Ramezani Rad, M. Mutations in the SAM domain of STE50 differentially influence the MAPK-mediated pathways for mating, filamentous growth and osmotolerance in Saccharomyces cerevisiae. *Mol. Genet. Genomics* **265**, 102–117 (2001).
19. Bardwell, L., Cook, J. G., Chang, E. C., Cairns, B. R. & Thorner, J. Signaling in the yeast pheromone response pathway: specific and high-affinity interaction of the mitogen-activated protein (MAP) kinases Kss1 and Fus3 with the upstream MAP

kinase kinase Ste7. (1996).
20. Flatauer, L. J., Zadeh, S. F. & Bardwell, L. Mitogen-activated protein kinases with distinct requirements for Ste5 scaffolding influence signaling specificity in Saccharomyces cerevisiae. *Mol Cell Biol* **25**, 1793–1803 (2005).
21. Roberts, C. J. *et al.* Signaling and circuitry of multiple MAPK pathways revealed by a matrix of global gene expression profiles. *Science* **287**, 873–880 (2000).
22. Harrison, R. & DeLisi, C. Condition specific transcription factor binding site characterization in Saccharomyces cerevisiae. *Bioinformatics* **18**, 1289–1296 (2002).
23. Cook, J. G., Bardwell, L., Kron, S. J. & Thorner, J. Two novel targets of the MAP kinase Kss1 are negative regulators of invasive growth in the yeast Saccharomyces cerevisiae. *Genes Dev* **10**, 2831–2848 (1996).
24. Chang, F. & Herskowitz, I. Identification of a gene necessary for cell cycle arrest by a negative growth factor of yeast: FAR1 is an inhibitor of a G1 cyclin, CLN2. *Cell* **63**, 999–1011 (1990).
25. MacKay, V. L. *et al.* Characterization of the Bar proteinase, an extracellular enzyme from the yeast Saccharomyces cerevisiae. *Adv. Exp. Med. Biol.* **306**, 161–172 (1991).
26. Schnell, J. D. & Hicke, L. Non-traditional functions of ubiquitin and ubiquitin-binding proteins. *J. Biol. Chem.* **278**, 35857–35860 (2003).
27. Dohlman, H. G. & Thorner, J. REGULATION OF G PROTEIN–INITIATED SIGNAL TRANSDUCTION IN YEAST: Paradigms and Principles. *http://dx.doi.org/10.1146/annurev.biochem.70.1.703*
28. White, J. ScienceDirect.com - Current Biology - Yeast mating: Getting close to membrane merger. *Current biology* (2001).
29. Apanovitch, D. M., Slep, K. C., Sigler, P. B. & Dohlman, H. G. Sst2 is a GTPase-activating protein for Gpa1: purification and characterization of a cognate RGS-Galpha protein pair in yeast. *Biochemistry* **37**, 4815–4822 (1998).
30. Garrison, T. R. *et al.* Feedback phosphorylation of an RGS protein by MAP kinase in yeast. *J. Biol. Chem.* **274**, 36387–36391 (1999).
31. Doi, K. *et al.* MSG5, a novel protein phosphatase promotes adaptation to pheromone response in S. cerevisiae. *EMBO J.* **13**, 61–70 (1994).
32. Ren, B. *et al.* Genome-Wide Location and Function of DNA Binding Proteins. *Science Signaling* **290**, 2306 (2000).
33. Elion, E. A. Pheromone response, mating and cell biology. *Curr Opin Microbiol* **3**, 573–581 (2000).
34. Mahanty, S. K., Wang, Y., Farley, F. W. & Elion, E. A. Nuclear shuttling of yeast scaffold Ste5 is required for its recruitment to the plasma membrane and activation of the mating MAPK cascade. *Cell* **98**, 501–512 (1999).
35. Huh, W.-K. *et al.* Global analysis of protein localization in budding yeast. *Nature* **425**, 686–691 (2003).
36. Wong, W. Location Determines Degradation. *Science Signaling* **2**, ec13–ec13 (2009).
37. Tyers, M. & Futcher, B. Far1 and Fus3 link the mating pheromone signal transduction pathway to three G1-phase Cdc28 kinase complexes. *Mol Cell Biol* **13**, 5659–5669 (1993).
38. Peter, M., Gartner, A., Horecka, J., Ammerer, G. & Herskowitz, I. FAR1 links the signal transduction pathway to the cell cycle machinery in yeast. *Cell* **73**, 747–760

(1993).
39. Elion, E. A., Satterberg, B. & Kranz, J. E. FUS3 phosphorylates multiple components of the mating signal transduction cascade: evidence for STE12 and FAR1. *Mol Biol Cell* **4**, 495–510 (1993).
40. Cherkasova, V., Lyons, D. M. & Elion, E. A. Fus3p and Kss1p control G1 arrest in Saccharomyces cerevisiae through a balance of distinct arrest and proliferative functions that operate in parallel with Far1p. *Genetics* **151**, 989–1004 (1999).
41. Jeoung, D. I. & Cross, F. The regulation of Clb5 kinase activity by mating factor. *Mol. Cells* **10**, 460–464 (2000).
42. Chen, T. & Kurjan, J. Saccharomyces cerevisiae Mpt5p interacts with Sst2p and plays roles in pheromone sensitivity and recovery from pheromone arrest. *Mol Cell Biol* **17**, 3429–3439 (1997).
43. Cherkasova, V. A., McCully, R., Wang, Y., Hinnebusch, A. & Elion, E. A. A Novel Functional Link between MAP Kinase Cascades and the Ras/cAMP Pathway that Regulates Survival. *Current biology* **13**, 1220–1226 (2003).
44. Oehlen, L. J. & Cross, F. R. G1 cyclins CLN1 and CLN2 repress the mating factor response pathway at Start in the yeast cell cycle. *Genes Dev* **8**, 1058–1070 (1994).
45. Oda, Y., Huang, K., Cross, F. R., Cowburn, D. & Chait, B. T. Accurate quantitation of protein expression and site-specific phosphorylation. *Proc Natl Acad Sci USA* **96**, 6591–6596 (1999).
46. Strickfaden, S. C. *et al.* A mechanism for cell-cycle regulation of MAP kinase signaling in a yeast differentiation pathway. *Cell* **128**, 519–531 (2007).
47. Winters, M. J., Lamson, R. E., Nakanishi, H., Neiman, A. M. & Pryciak, P. M. A membrane binding domain in the ste5 scaffold synergizes with gbetagamma binding to control localization and signaling in pheromone response. *Mol. Cell* **20**, 21–32 (2005).
48. Shimomura, O., JOHNSON, F. H. & SAIGA, Y. Extraction, purification and properties of aequorin, a bioluminescent protein from the luminous hydromedusan, Aequorea. *J Cell Comp Physiol* **59**, 223–239 (1962).
49. Shimomura, O. Structure of the chromophore of Aequorea green fluorescent protein. *FEBS Lett* **104**, 220–222 (1979).
50. Morise, H., Shimomura, O., Johnson, F. H. & Winant, J. Intermolecular energy transfer in the bioluminescent system of Aequorea. *Biochemistry* **13**, 2656–2662 (1974).
51. Prasher, D. C., Eckenrode, V. K., Ward, W. W., Prendergast, F. G. & Cormier, M. J. Primary structure of the Aequorea victoria green-fluorescent protein. *Gene* **111**, 229–233 (1992).
52. Tsien, R. The green fluorescent protein. *Annu Rev Biochem* (1998).
53. Shaner, N. C., Steinbach, P. A. & Tsien, R. Y. A guide to choosing fluorescent proteins. *Nat Methods* **2**, 905–909 (2005).
54. Campbell, R. E. *et al.* A monomeric red fluorescent protein. *Proc Natl Acad Sci USA* **99**, 7877–7882 (2002).
55. Shaner, N. C. *et al.* Improved monomeric red, orange and yellow fluorescent proteins derived from Discosoma sp. red fluorescent protein. *Nat Biotechnol* **22**, 1567–1572 (2004).
56. Cubitt, A. B. *et al.* Understanding, improving and using green fluorescent proteins.

Trends Biochem Sci **20**, 448–455 (1995).
57. Taylor, R. J. *et al.* Dynamic analysis of MAPK signaling using a high-throughput microfluidic single-cell imaging platform. *Proc Natl Acad Sci USA* **106**, 3758–3763 (2009).
58. Liu, Q. *et al.* SCFCdc4 enables mating type switching in yeast by cyclin-dependent kinase-mediated elimination of the Ash1 transcriptional repressor. *Mol Cell Biol* **31**, 584–598 (2011).
59. Bertrand, E. *et al.* Localization of ASH1 mRNA particles in living yeast. *Mol. Cell* **2**, 437–445 (1998).
60. Elowitz, M. B., Levine, A. J., Siggia, E. D. & Swain, P. S. Stochastic gene expression in a single cell. *Science* **297**, 1183–1186 (2002).
61. Elowitz, M. B. & Leibler, S. A synthetic oscillatory network of transcriptional regulators. *Nature* **403**, 335–338 (2000).
62. Gordon, A. *et al.* Single-cell quantification of molecules and rates using open-source microscope-based cytometry. *Nat Methods* **4**, 175–181 (2007).
63. Yang, Q., Mettetal, J. & van Oudenaarden, A. Heritable stochastic switching revealed by single-cell genealogy. *PLoS Biol* **5**, e239 (2006).
64. Ty M Thomson, K. R. B. A. B. T. L. D. P. O. R. R. C. Y. A. G. A. C.-L. D. E. R. B. Scaffold number in yeast signaling system sets tradeoff between system output and dynamic range. *Proc Natl Acad Sci USA* **108**, 20265 (2011).
65. Dittrich, P. & Manz, A. Lab-on-a-chip: microfluidics in drug discovery. *Nature Reviews Drug Discovery* (2006).
66. Qin, D., Xia, Y. & Whitesides, G. Rapid Prototyping of Complex Structures with Feature Sizes Larger than 20 mm. *Advanced ...* (1996).
67. Duffy, D. C., McDonald, J. C., Schueller, O. J. A. & Whitesides, G. M. Rapid Prototyping of Microfluidic Systems in Poly(dimethylsiloxane). *Anal Chem* **70**, 4974–4984 (1998).
68. McDonald, J. C. *et al.* Fabrication of microfluidic systems in poly(dimethylsiloxane). *Electrophoresis* **21**, 27–40 (2000).
69. Whitesides, G. & Ostuni, E. Soft lithography in biology and biochemistry. *Annual review of ...* (2001).
70. Anderson, J. R. *et al.* Fabrication of topologically complex three-dimensional microfluidic systems in PDMS by rapid prototyping. *Anal Chem* **72**, 3158–3164 (2000).
71. Unger, M. A., Chou, H. P., Thorsen, T., Scherer, A. & Quake, S. R. Monolithic microfabricated valves and pumps by multilayer soft lithography. *Science* **288**, 113–116 (2000).
72. Thorsen, T. Microfluidic Large-Scale Integration. *Science* **298**, 580–584 (2002).
73. Hansen, C. & Quake, S. R. Microfluidics in structural biology: smaller, faster em leader better. *Curr Opin Struct Biol* **13**, 538–544 (2003).
74. Balaban, N. Q., Merrin, J., Chait, R., Kowalik, L. & Leibler, S. Bacterial persistence as a phenotypic switch. *Science* **305**, 1622–1625 (2004).
75. Balagaddé, F. K., You, L., Hansen, C. L., Arnold, F. H. & Quake, S. R. Long-term monitoring of bacteria undergoing programmed population control in a microchemostat. *Science* **309**, 137–140 (2005).
76. Groisman, A. *et al.* A microfluidic chemostat for experiments with bacterial and

yeast cells. *Nat Methods* **2**, 685–689 (2005).
77. Tesla, N. Valvular Conduit. (1920).
78. Stricker, J. *et al.* A fast, robust and tunable synthetic gene oscillator. *Nature* **456**, 516–519 (2008).
79. Grilly, C., Stricker, J., Pang, W. L., Bennett, M. R. & Hasty, J. A synthetic gene network for tuning protein degradation in Saccharomyces cerevisiae. *Mol Syst Biol* **3**, 127 (2007).
80. Cookson, N. A., Cookson, S. W., Tsimring, L. S. & Hasty, J. Cell cycle-dependent variations in protein concentration. *Nucleic acids research* **38**, 2676–2681 (2010).
81. Bennett, M. R. *et al.* Metabolic gene regulation in a dynamically changing environment. *Nature* **454**, 1119–1122 (2008).
82. Charvin, G., Cross, F. R. & Siggia, E. D. A microfluidic device for temporally controlled gene expression and long-term fluorescent imaging in unperturbed dividing yeast cells. *PLoS ONE* **3**, e1468 (2008).
83. Charvin, G., Cross, F. R. & Siggia, E. D. Forced periodic expression of G1 cyclins phase-locks the budding yeast cell cycle. *Proc Natl Acad Sci USA* **106**, 6632–6637 (2009).
84. Di Talia, S. *et al.* Daughter-specific transcription factors regulate cell size control in budding yeast. *PLoS Biol* **7**, e1000221 (2009).
85. Lu, Y. & Cross, F. R. Periodic Cyclin-Cdk Activity Entrains an Autonomous Cdc14 Release Oscillator. *Cell* **141**, 268–279 (2010).
86. Rowat, A. C., Bird, J. C., Agresti, J. J., Rando, O. J. & Weitz, D. A. Tracking lineages of single cells in lines using a microfluidic device. *Proc Natl Acad Sci USA* **106**, 18149–18154 (2009).
87. Mettetal, J. T., Muzzey, D., Gomez-Uribe, C. & van Oudenaarden, A. The Frequency Dependence of Osmo-Adaptation in Saccharomyces cerevisiae. *Science* **319**, 482–484 (2008).
88. Hong, J. W., Studer, V., Hang, G., Anderson, W. F. & Quake, S. R. A nanoliter-scale nucleic acid processor with parallel architecture. *Nat Biotechnol* **22**, 435–439 (2004).
89. Melin, J. & Quake, S. R. Microfluidic Large-Scale Integration: The Evolution of Design Rules for Biological Automation. *Annu. Rev. Biophys. Biomol. Struct.* **36**, 213–231 (2007).
90. Jeon, N. *et al.* Generation of solution and surface gradients using microfluidic systems. *Langmuir* **16**, 8311–8316 (2000).
91. Jeon, N., Baskaran, H. & Dertinger, S. Neutrophil chemotaxis in linear and complex gradients of interleukin-8 formed in a microfabricated device. *Nat. ...* (2002).
92. Mao, H., Cremer, P. & Manson, M. A sensitive, versatile microfluidic assay for bacterial chemotaxis. *Proceedings of the ...* (2003).
93. Delbrück, M. Statistical Fluctuations in Autocatalytic Reactions. *J. Chem. Phys.* **8**, 120 (1940).
94. Schrödinger, E. *What is Life?* (Cambridge University Press: 1944).
95. JACOB, F. & MONOD, J. Genetic regulatory mechanisms in the synthesis of proteins. *J. Mol. Biol.* **3**, 318–356 (1961).
96. Benzer, S. Induced synthesis of enzymes in bacteria analyzed at the cellular level. *Biochim Biophys Acta* **11**, 383–395 (1953).
97. Aaron Novick, M. W. ENZYME INDUCTION AS AN ALL-OR-NONE

PHENOMENON. *Proc Natl Acad Sci USA* **43**, 553 (1957).
98. Spudich, J. & Koshland, D., Jr Non-genetic individuality: chance in the single cell. *Nature* (1976).
99. Gillespie, D. Exact stochastic simulation of coupled chemical reactions - The Journal of Physical Chemistry (ACS Publications). *The journal of physical chemistry* (1977).
100. McAdams, H. H. & Arkin, A. Stochastic mechanisms in gene expression. *Proc Natl Acad Sci USA* **94**, 814–819 (1997).
101. Arkin, A., Ross, J. & McAdams, H. H. Stochastic kinetic analysis of developmental pathway bifurcation in phage lambda-infected Escherichia coli cells. *Genetics* **149**, 1633–1648 (1998).
102. Becskei, A. & Serrano, L. Engineering stability in gene networks by autoregulation. *Nature* **405**, 590–593 (2000).
103. Ozbudak, E. M., Thattai, M., Kurtser, I., Grossman, A. D. & van Oudenaarden, A. Regulation of noise in the expression of a single gene. *Nat Genet* **31**, 69–73 (2002).
104. Thattai, M. & van Oudenaarden, A. Intrinsic noise in gene regulatory networks. *Proc Natl Acad Sci USA* **98**, 8614–8619 (2001).
105. Blake, W. J., KAErn, M., Cantor, C. R. & Collins, J. J. Noise in eukaryotic gene expression. *Nature* **422**, 633–637 (2003).
106. Raser, J. M. & O'Shea, E. K. Control of stochasticity in eukaryotic gene expression. *Science* **304**, 1811–1814 (2004).
107. Raj, A., Peskin, C. S., Tranchina, D., Vargas, D. Y. & Tyagi, S. Stochastic mRNA synthesis in mammalian cells. *PLoS Biol* **4**, e309 (2006).
108. Becskei, A., Kaufmann, B. B. & van Oudenaarden, A. Contributions of low molecule number and chromosomal positioning to stochastic gene expression. *Nat Genet* **37**, 937–944 (2005).
109. Cai, L., Friedman, N. & Xie, X. S. Stochastic protein expression in individual cells at the single molecule level. *Nature* **440**, 358–362 (2006).
110. Yu, J., Xiao, J., Ren, X., Lao, K. & Xie, X. S. Probing gene expression in live cells, one protein molecule at a time. *Science* **311**, 1600–1603 (2006).
111. Golding, I., Paulsson, J., Zawilski, S. M. & Cox, E. C. Real-Time Kinetics of Gene Activity in Individual Bacteria. *Cell* **123**, 1025–1036 (2005).
112. Huh, D. & Paulsson, J. Non-genetic heterogeneity from stochastic partitioning at cell division. *Nat Genet* **43**, 95–100 (2011).
113. Rosenfeld, N., Young, J. W., Alon, U., Swain, P. S. & Elowitz, M. B. Gene regulation at the single-cell level. *Science* **307**, 1962–1965 (2005).
114. Huh, D. & Paulsson, J. Random partitioning of molecules at cell division. *Proc Natl Acad Sci USA* (2011).doi:10.1073/pnas.1013171108
115. Hilfinger, A. & Paulsson, J. Separating intrinsic from extrinsic fluctuations in dynamic biological systems. *Proceedings of the National Academy of Sciences* **108**, 12167–12172 (2011).
116. Raj, A. & van Oudenaarden, A. Nature, nurture, or chance: stochastic gene expression and its consequences. *Cell* (2008).
117. Pedraza, J. M. & van Oudenaarden, A. Noise propagation in gene networks. *Science* **307**, 1965–1969 (2005).
118. Spencer, S. L., Gaudet, S., Albeck, J. G., Burke, J. M. & Sorger, P. K. Non-genetic origins of cell-to-cell variability in TRAIL-induced apoptosis. *Nature* **459**, 428–432

(2009).
119. Neves, das, R. P. *et al.* Connecting variability in global transcription rate to mitochondrial variability. *PLoS Biol* **8**, e1000560 (2010).
120. Gefen, O., Gabay, C., Mumcuoglu, M., Engel, G. & Balaban, N. Q. Single-cell protein induction dynamics reveals a period of vulnerability to antibiotics in persister bacteria. *Proc Natl Acad Sci USA* **105**, 6145–6149 (2008).
121. Avi Ashkenazi, R. S. H. To kill a tumor cell: the potential of proapoptotic receptor agonists. *The Journal of Clinical Investigation* **118**, 1979 (2008).
122. Niepel, M., Spencer, S. L. & Sorger, P. K. Non-genetic cell-to-cell variability and the consequences for pharmacology. *Curr Opin Chem Biol* **13**, 556–561 (2009).
123. Paulsson, J., Berg, O. G. & Ehrenberg, M. Stochastic focusing: fluctuation-enhanced sensitivity of intracellular regulation. *Proc Natl Acad Sci USA* **97**, 7148–7153 (2000).
124. Maamar, H., Raj, A. & Dubnau, D. Noise in gene expression determines cell fate in Bacillus subtilis. *Science* **317**, 526–529 (2007).
125. Süel, G. M., Kulkarni, R. P., Dworkin, J., Garcia-Ojalvo, J. & Elowitz, M. B. Tunability and noise dependence in differentiation dynamics. *Science* **315**, 1716–1719 (2007).
126. Janke, C. *et al.* A versatile toolbox for PCR-based tagging of yeast genes: new fluorescent proteins, more markers and promoter substitution cassettes. *Yeast* **21**, 947–962 (2004).
127. Sheff, M. A. & Thorn, K. S. Optimized cassettes for fluorescent protein tagging inSaccharomyces cerevisiae. *Yeast* **21**, 661–670 (2004).
128. Hunter, J. D. Matplotlib: A 2D Graphics Environment. *Comput. Sci. Eng.* **9**, 90–95 (2007).
129. Bardwell, L. *et al.* Repression of yeast Ste12 transcription factor by direct binding of unphosphorylated Kss1 MAPK and its regulation by the Ste7 MEK. *Genes Dev* **12**, 2887–2898 (1998).
130. Swain, P. & et al Intrinsic and extrinsic contributions to stochasticity in gene expression. *Proceedings of the ...* (2002).
131. Hartwell, L. H. & Unger, M. W. Unequal division in Saccharomyces cerevisiae and its implications for the control of cell division. *J Cell Biol* **75**, 422–435 (1977).
132. Fisher, R. A. Frequency distribution of the values of the correlation coefficient in samples from an indefinitely large population. *Biometrika* **10**, 507–521 (1915).
133. Bishop, A. C. *et al.* A chemical switch for inhibitor-sensitive alleles of any protein kinase. *Nature* **407**, 395–401 (2000).
134. Gartner, A. *et al.* Pheromone-dependent G1 cell cycle arrest requires Far1 phosphorylation, but may not involve inhibition of Cdc28-Cln2 kinase, in vivo. *Mol Cell Biol* **18**, 3681–3691 (1998).
135. Ramezani-Rad, M. The role of adaptor protein Ste50-dependent regulation of the MAPKKK Ste11 in multiple signalling pathways of yeast. *Curr Genet* **43**, 161–170 (2003).
136. Laabs, T. L. *et al.* ACE2 is required for daughter cell-specific G1 delay in Saccharomyces cerevisiae. *Proc Natl Acad Sci USA* **100**, 10275–10280 (2003).
137. Ramezani Rad, M., Jansen, G., Bühring, F. & Hollenberg, C. P. Ste50p is involved in regulating filamentous growth in the yeast Saccharomyces cerevisiae and

associates with Ste11p. *Mol. Gen. Genet.* **259**, 29–38 (1998).
138. Tatebayashi, K. *et al.* Adaptor functions of Cdc42, Ste50, and Sho1 in the yeast osmoregulatory HOG MAPK pathway. *EMBO J.* **25**, 3033–3044 (2006).
139. Slaughter, B. D., Smith, S. E. & Li, R. Symmetry breaking in the life cycle of the budding yeast. *Cold Spring Harb Perspect Biol* **1**, a003384 (2009).
140. Colman-Lerner, A., Chin, T. E. & Brent, R. Yeast Cbk1 and Mob2 activate daughter-specific genetic programs to induce asymmetric cell fates. *Cell* **107**, 739–750 (2001).
141. Weiss, E. L. *et al.* The Saccharomyces cerevisiae Mob2p-Cbk1p kinase complex promotes polarized growth and acts with the mitotic exit network to facilitate daughter cell-specific localization of Ace2p transcription factor. *J Cell Biol* **158**, 885–900 (2002).
142. Mazanka, E. *et al.* The NDR/LATS Family Kinase Cbk1 Directly Controls Transcriptional Asymmetry. *PLoS Biol* **6**, e203 (2008).
143. Geyer, C. R., Colman-Lerner, A. & Brent, R. "Mutagenesis" by peptide aptamers identifies genetic network members and pathway connections. *Proc Natl Acad Sci USA* **96**, 8567–8572 (1999).
144. Gehlen, L., Nagai, S., Shimada, K. & Meister, P. Nuclear Geometry and Rapid Mitosis Ensure Asymmetric Episome Segregation in Yeast 10.1016/j.cub.2010.12.016 : Current Biology | ScienceDirect.com. *Current biology* (2010).
145. Lecault, V. *et al.* High-throughput analysis of single hematopoietic stem cell proliferation in microfluidic cell culture arrays. *Nat Methods* **8**, 581–586 (2011).
146. Falconnet, D. *et al.* High-throughput tracking of single yeast cells in a microfluidic imaging matrix. *Lab Chip* **11**, 466–473 (2010).
147. Li, G.-W. & Xie, X. S. Central dogma at the single-molecule level in living cells. *Nature* **475**, 308–315 (2011).
148. Paulsson, J. Models of stochastic gene expression. *Physics of life reviews* (2005).
149. Bessard, A. *et al.* RNAi-mediated ERK2 knockdown inhibits growth of tumor cells in vitro and in vivo. *Oncogene* **27**, 5315–5325 (2008).